JCU ePrints

This file is part of the following reference:

New, Brian (2006) *Controls of copper and gold distribution in the Kucing Liar deposit, Ertsberg mining district, West Papua, Indonesia.* **PhD thesis, James Cook University.**

Access to this file is available from:

http://eprints.jcu.edu.au/2083

JCU
JAMES COOK UNIVERSITY

7 Stable isotope geochemistry

Stable isotope data place constraints on source reservoir(s) for water in hydrothermal fluids. The data in Chapters 2 and 3 enable these results to be assessed in terms of their temporal and spatial context. This can be used to establish the evolutionary path taken by hydrothermal fluids and the physical processes which occurred during their migration through wall rocks.

Pure mineral samples were collected from as many different minerals and paragenetic assemblages as was available and submitted for isotopic analysis. Individual grains were picked from crushed sample material and separated using a fine brush. Analyses of each sample are converted from mineral to fluid compositions by way of experimentally and theoretically derived fractionation equations for the relevant isotopes in each mineral. This section documents the results of stable isotope analyses for the purposes of determining the sources of hydrothermal waters. Small pieces of rock sample were crushed in hand mortar and pestle until the majority of sample was less than $500\mu m$. Individual crystals of each mineral were separated using fine brushes, producing 50 separates samples of 16 mineral phases which were analysed for oxygen isotopes, 13 (6 mineral phases) for hydrogen isotopes, 13 (7 mineral phases) for sulphur isotopes and 3 (2 mineral phases) for carbon isotopes. Oxygen and carbon isotope analyses were submitted to Monash University in Melbourne, Australia, samples for hydrogen analyses were sent to Adrian Boyce the SUERRC East Kilbride Research Park in Glasgow, Scotland and samples for sulphur analyses sent to Sue Golding at the University of Queensland, Brisbane, Australia. The analytical methods are documented in Appendix VII. The oxygen and hydrogen compositions are reported relative to Standard Mean Ocean Water (V-SMOW). Sulphur is recorded as relative to Cañon Diablo Troilite (CDT). Carbon is reported as relative to calcite from the Peedee Belemnite (PDB). Calculated fluid compositions are then compared to published ranges for primary magmatic water, water derived from metamorphism, and local meteoric water in order to assess the origins of Kucing Liar fluids.

_____

7.1 ISOTOPIC ANALYSES

A total of 63 mineral separates (23 different minerals) from 43 hand specimens were collected (Table 7-1). Most of the samples for stable isotope analysis were collected from a single drill station (KL32) in order to apply consistent spatial context to each sample. Additional samples off this section were dictated by the availability of material or a specific paragenetic association. All minerals except talc, calcite, sphalerite and galena were analysed from more than one sample. A deliberate effort was also made to collect a variety of the modes of development of minerals as documented in Chapter 2 (e.g. pervasive alteration, selvedge alteration of fracture infill). The collection includes samples representing both alteration and infill for single minerals (K-feldspar, biotite, magnetite, anhydrite), plus analyses of the same phase from different host units and lithology. Multiple pure samples of various minerals from each paragenetic stage were collected for oxygen isotope analysis. Only six hydroxyl-bearing minerals were analysed for hydrogen isotope composition. For green phlogopite, muscovite and serpentine only one sample was used. Nevertheless, each Group of the paragenesis is represented by at least one hydrogen isotope analysis (Table 7-1). Only Groups II and III have been assessed for sulphur isotope composition via pure samples of anhydrite, pyrite, chalcopyrite and covellite. A variety of styles of anhydrite and pyrite occurrence were sampled but only two samples each of chalcopyrite and covellite are included.

7.1.1   Results of analyses

Multiple analyses of individual mineral phases define single populations of $\delta^{18}O$ spread over narrow ranges of 2-3‰ except for K-feldspar, tremolite, anhydrite, which are bimodal, and quartz alteration which has a large range of $\delta^{18}O$ (6-12‰). Most $\delta^{18}O_{MINERAL}$ values lie between 0 and 12‰, with only dolomite samples having outlying values at 22‰ (Figure 7-1). Earlier formed minerals display narrower ranges of $\delta^{18}O$ than later formed minerals (Figure 7-1a). Skarn and potassic minerals (diopside, garnet and humite as well as biotite and quartz veins) all display narrow ranges of 1-3‰. Two samples of K-feldspar have quite different values. Magnetite has a

_____

slightly broader range of 4‰ while tremolite-actinolite values are divided into 3-4‰ and 7-8‰ (Table 7-1). δD ranges between –275 and –100‰, with an apparent mode between –150 and –175‰ (Figure 7-1b). Two humite samples display a large difference in δD, with the single green phlogopite sample lying between them. Three biotite samples have a narrow range of δD from –180 to –200 (Table 7-1). δ^{34}S values form two populations, respectively comprising sulphate and sulphide species (Figure 7-1c). Anhydrite samples have a narrower range of δ^{34}S (2‰) relative to δ^{18}O (3.5‰) for the same samples (Table 7-1). The six samples of pyrite have a large but continuous range of δ^{34}S between –8 and 2‰. The lowest of these (–6.2‰), is from a sample of fine pyrite, whereas δ^{34}S in coarse pyrite from the same sample is –4‰ and similar to other samples of coarse pyrite (Table 7-1). Only three samples of chalcopyrite and two of covellite were analysed and have very different values of δ^{34}S, within the same range as pyrite. Galena and sphalerite have similar δ^{34}S equivalent to the highest pyrite and chalcopyrite values.

Lithology is not a significant factor in the isotopic composition of hydrothermal minerals. Diopside samples collected from shale and limestone wall rocks have identical oxygen compositions, as do biotite samples from shale and fault zone and quartz veins hosted by shale, sandstone and fault zones (Table 7-1). Similarly, although quartz alteration samples have a wider range of compositions than skarn minerals, the variation is not related to wall rock lithology. Limited data from K-feldspar might suggest some lithological control though the data are limited to two samples (Table 7-1). Textural variations in mineral development have a minor effect on mineral compositions where some minerals display variability in isotope chemistry that may be related to mode of occurrence. For example, anhydrite δ^{18}O values for alteration are significantly higher (2.8 and 4.8‰) than infill (1.2‰) (Table 7-1). However, there appears to be no textural characteristic (grainsize or colour) or growth form (infill or alteration) of tremolite-actinolite that is coincident with the variable δ^{18}O, nor a single textural characteristic that parallels the large range of δ^{18}O of quartz alteration.

Table 7-1 Stable isotope samples and results (‰)

Drill hole	Depth	Lith	Mineral	Form	Group	$\delta^{18}O$	δD	$\delta^{34}S$	$\delta^{13}C$
KLS3-1	1420.7	lst	dolomite	Alt	Host	22.0			1.3
KL38-05	814.1	lst	dolomite	Alt	Host	22.5			2.5
KL32-03	388.3	shl	diopside	Alt	I	4-4			
KL32-09	342.9	lst	diopside	Alt	I	4-8			
KL32-04	247.5	lst	diopside	Alt	I	6.0			
KL32-07	394.5	shl	diopside	Alt	I	6.1			
KL38-05	708.2	lst	diopside	Alt	I	6.5			
KL26-08	384-4	shl	garnet (green)	Alt	I	4.1			
KL32-03	381.5	shl	garnet (green)	Alt	I	4.2			
KL26-08	384-4	shl	garnet (red)	Alt	I	4.5			
KL16-09	57.2	lst	humite	Alt	I	3.0	-257		
KL26-08	318.0	lst	humite	Alt	I	3.3	-168		
KL28-01	360.3	unk	green phlogopite	Alt	I	6.1	-217		
KL32-08	331.0	lst	green phlogopite	Alt	I	7.0			
KL28-01	360.3	unk	K-feldspar	Inf	II	8.0			
KL38-05	711.5	shl	K-feldspar	Alt	II	12.0			
KL32-07	601.0	sst	quartz (vein)	Inf	II	10.4			
KL32-08	480.1	shl	quartz (vein)	Inf	II	10.5			
KL32-01	263.8	unk	quartz (vein)	Inf	II	11.4			
KL32-07	349.5	shl	quartz (vein)	Inf	II	11.5			
KL32-07	342.2	lst	magnetite	Alt	II	0.9			
KL28-01	272.9	lst	magnetite	Alt	II	1.3			
KL32-03	416.9	unk	magnetite	Alt	II	1.6			
KL32-05	313.9	lst	magnetite	Alt	II	2.6			
KL32-07	349.5	shl	magnetite	Inf	II	3.1			
KL20-09	464-3	shl	biotite	Inf	II	3.4	-195		
KL32-05	652.4	shl	biotite	Inf	II	4.0	-204		
KL32-05	539.6	unk	biotite	Alt	II	4.3	-181		
KL32-08	410.0	lst	serpentine	Alt	III	6.1			
KL32-08	331.0	lst	serpentine	Alt	III	6.2	-154		
KL32-05	539.6	unk	tremolite	Alt	II	3.2	-181		
KL32-04	500.8	lst	tremolite	Alt	II	3.4	-110		
KL32-08	357.1	lst	tremolite	Alt	II	3.4	-154		
KL38-05	638.9	lst	tremolite	Alt	II	7.0			
KL28-01	266.9	lst	tremolite	Alt	II	7.9	-159		
KL32-07	329.0	lst	talc	Alt	III	4.9			

Hole	Depth	Lith	Mineral	Form	Group	$\delta^{18}O$	δD	$\delta^{34}S$	$\delta^{13}C$
KL32-07	342.2	lst	anhydrite	Inf	III	1.2		11.6	
KL32-08	410.0	lst	anhydrite	Alt	III	2.8		9.5	
KL32-08	480.1	shl	anhydrite	Alt	III	4.8		10.2	
KL32-03	416.9	unk	anhydrite	Inf	III	1.2		10.7	
KL38-05	224-4	lst	quartz (alt)	Alt	III	6.3			
KL32-05	339.2	shl	quartz (alt)	Alt	III	7.1			
KL30-01	222.1	lst	quartz (alt)	Alt	III	8.4			
KL32-03	354.3	shl	quartz (alt)	Alt	III	9.9			
KL32-05	296.3	lst	quartz (alt)	Alt	III	10.0			
KL32-05	706.7	sst	quartz (alt)	Alt	III	11.0			
KL32-01	254-7	unk	quartz (alt)	Alt	III	11.3			
KL32-01	254-7	unk	muscovite	Inf	III	6.2			
KL32-08	454-9	shl	muscovite	Alt	III	6.9	-105		
KL32-03	426.6	unk	calcite	Inf	IV	9.3			0.4
KL32-05	539.6	unk	chalcopyrite	Inf	IV			-3.8	
KL32-03	416.9	unk	chalcopyrite	Inf	IV			-2.9	
KL28-01	266.9	lst	chalcopyrite	Alt	IV			2.4	
KL28-01	266.9	lst	pyrite	Alt	IV			-2.0	
KL32-05	539.6	unk	pyrite	Inf	IV			-3.1	
KL32-03	426.6	unk	pyrite (fine)	Alt	IV			-6.2	
KL32-03	426.6	unk	pyrite (coarse)	Alt	IV			-4.0	
KL32-08	454-9	shl	pyrite (coarse)	Inf	IV			-2.7	
KL32-01	254-7	unk	pyrite (coarse)	Alt	IV			0.1	
KL20-05	237.8	lst	covellite	Inf	IV			-6.1	
KL42-02	100.2	sst	covellite	Inf	IV			-0.1	
KL42-05	337.0	lst	galena	Inf	IV			1.3	
KL42-05	337.0	lst	sphalerite	Inf	IV			2.4	

Table 7-1 Stable isotope samples and results (cont.)

Abbreviations: lst = limestone, shl = shale, sst = sandstone, unk = unknown; Alt = alteration, Inf = infill. The measured isotope ratios are calculated as a shift from zero (δ) reported in permil (‰) deviation from standard (V-SMOW for oxygen and hydrogen, CDT for sulphur and V-PDB for carbon). Analytical precision is ±0.2‰ in silicates and ±0.1‰ in carbonates in for oxygen, ±2‰ for hydrogen and ±0.3‰ for sulphur.
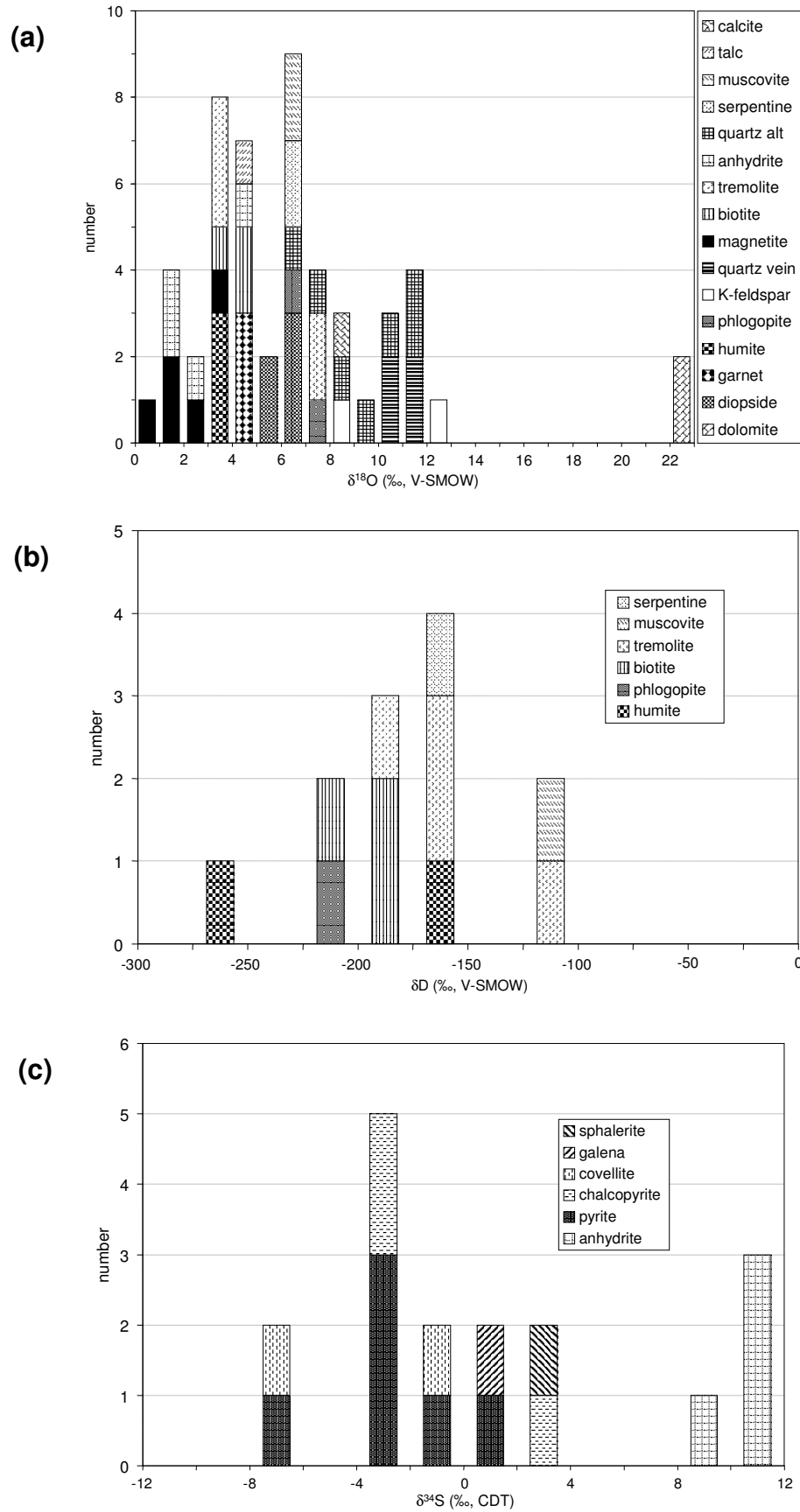
Figure 7-1 Histograms showing analysed oxygen, hydrogen and sulphur isotope ratios

_____

7.1.2   Fluid compositions

The isotopic fractionation between a mineral and a coexisting fluid is calculated by determining the difference (Δ) in isotopic compositions (δ) of the mineral (substance) and water thus (e.g.):

$$\Delta^{18}O_{\text{MINERAL-FLUID}} = \delta^{18}O_{\text{MINERAL}} - \delta^{18}O_{\text{FLUID}}$$

For the selected minerals from Kucing Liar, the value of Δ is calculated for ^{18}O, D, and ^{34}S from the equations listed in Table 7-3, Table 7-4 and Table 7-5 which allow for the calculation of the isotopic composition of fluids. Calculation of Δ values requires the temperature of mineral formation for input into the equilibrium equations. Estimated temperatures of formation for each mineral are listed in Table 7-2 and are based on constraints from phase equilibria (Group I, II and III) and fluid inclusion homogenisation temperatures (Group II and III). While the temperatures may be broad estimates only, the slope of the curves in the vicinity of the temperatures are so slight that in many cases a difference between assumed and real temperatures of ±100°C will only result in a change of calculated $\Delta_{\text{MINERAL-FLUID}}$ of ±2‰ and not greater than ±5‰ in the most extreme cases (dolomite, anhydrite, serpentine, talc, calcite).

Table 7-2 Temperatures used for calculating fluid isotope compositions

Mineral	Estimated T (°C)
Dolomite: $CaMg(CO_3)_2$	300
Diopside: $CaMgSi_2O_6$	650
Andradite: $Ca_3Fe_2Si_3O_{12}$	650
Grossular: $Ca_3Al_2Si_3O_{12}$	650
Humite: $(Mg,Fe)_7(SiO_4)_3(F,OH)_2$	650
Phlogopite-OH: $KMg_3AlSi_3O_{10}(OH)_2$	550
K-feldspar: $KAlSi_3O_8$	550
Quartz veins: SiO_2	700
Magnetite: Fe_3O_4	450
Biotite: $K(Mg,Fe)_3(Si_3Al)O_{10}(OH,F)_2$	550
Tremolite: $Ca_2Mg_5Si_8O_{22}(OH)_2$	450
Serpentine: $Mg_3Si_2O_5(OH)_4$	350
Anhydrite: $CaSO_4$	400
Quartz alteration: SiO_2	350
Muscovite: $KAl_3Si_3O_{10}(OH)_2$	350
Talc: $Mg_3Si_4O_{10}(OH)_2$	350
Calcite: $CaCO_3$	350
Pyrite: FeS_2	350
Chalcopyrite: $CuFeS_2$	350
Covellite: CuS	350
Sphalerite: ZnS	300
Galena: PbS	300

Temperatures for quartz veins and quartz alteration are based on directly measured homogenisation temperatures for fluid inclusions while covellite is assumed from measurement of paragenetically associated fluorite-hosted inclusions (see Chapter 6). All other temperatures are based on either paragenetic associations or published information for similar styles of alteration in skarn deposits. The assumed temperatures for all other of the minerals either lie on a low slope section of the fractionation curve or are well constrained such that the amount of error introduced is expected to be low. Calculations for the range of ±50°C were also completed to assess the reliability of the derived data, these figures emphasise that uncertainties in the temperatures used to calculate fractionations will generally produce small errors in the estimated fluid compositions and could not affect the conclusions in any substantive way.

Table 7-3 Mineral-H_2O fractionation equations for oxygen (Temperature (T) is in Kelvin)

| Mineral	Fractionation equation	Reference
Dolomite: $CaMg(CO_3)_2$	$3.06 \times 10^6 / (T)^2 + 10^3 / T - 3.24$	Matthews and Katz (1977)
Diopside: $CaMgSi_2O_6$	$3.92 \times 10^6 / (T)^2 - 8.43 \times 10^3 / T + 2.4$	Zheng (1993)
Andradite: $Ca_3Fe_2Si_3O_{12}$	$3.76 \times 10^6 / (T)^2 - 9.05 \times 10^3 / T + 2.52$	Zheng (1993)
Grossular: $Ca_3Al_2Si_3O_{12}$	$3.74 \times 10^6 / (T)^2 - 9.11 \times 10^3 / T + 2.52$	Zheng (1993)
Humite: $(Mg,Fe)_7(SiO_4)_3(F,OH)_2$	$3.77 \times 10^6 / (T)^2 - 9.01 \times 10^3 / T + 2.51$	Zheng (1993)
Phlogopite: $KMg_3AlSi_3O_{10}(OH)_2$	$3.86 \times 10^6 / (T)^2 - 8.68 \times 10^3 / T + 2.45$	Zheng (1993)
K-feldspar: $KAlSi_3O_8$	$4.32 \times 10^6 / (T)^2 - 6.27 \times 10^3 / T + 2.0$	Zheng (1993)
Quartz: SiO_2	$4.48 \times 10^6 / (T)^2 - 4.77 \times 10^3 / T + 1.71$	Zheng (1993)
Magnetite: Fe_3O_4	$3.02 \times 10^6 / (T)^2 - 12.0 \times 10^3 / T + 3.31$	Zheng (1993)
Biotite: $K(Mg,Fe)_3(Si_3Al)O_{10}(OH,F)_2$	$3.84 \times 10^6 / (T)^2 - 8.76 \times 10^3 / T + 2.46$	Zheng (1993)
Tremolite: $Ca_2Fe_5Si_8O_{22}(OH)_2$	$3.95 \times 10^6 / (T)^2 - 8.28 \times 10^3 / T + 2.38$	Zheng (1993)
Serpentine: $Mg_3Si_2O_5(OH)_4$	$3.99 \times 10^6 / (T)^2 - 8.12 \times 10^3 / T + 2.35$	Zheng (1993)
Anhydrite: $CaSO_4$	$3.21 \times 10^6 / (T)^2 + 10^3 / T - 4.72$	Chiba et al. (1981)
Muscovite: $KAl_3Si_3O_{10}(OH)_2$	$4.1 \times 10^6 / (T)^2 - 7.61 \times 10^3 / T + 2.25$	Zheng (1993)
Talc: $Mg_3Si_4O_{10}(OH)_2$	$4.2 \times 10^6 / (T)^2 - 7.04 \times 10^3 / T + 2.14$	Zheng (1993)
Calcite: $CaCO_3$	$4.01 \times 10^6 / (T)^2 - 4.66 \times 10^3 / T - 0.06$	Zheng (1993)

Table 7-4 Mineral-H_2O fractionation equations for hydrogen (Temperature (T) is in Kelvin)

Mineral	Fractionation equation	Reference
Phlogopite: $KMg_3AlSi_3O_{10}(OH)_2$	$-22.4 \times 10^6 / (T)^2 + 10^3 / T + 27.1$	Suzuoki and Epstein (1976)
Biotite: $K(Mg,Fe)_3(Si_3Al)O_{10}(OH,F)_2$	$-21.3 \times 10^6 / (T)^2 + 10^3 / T - 2.8$	Suzuoki and Epstein (1976)
Tremolite: $Ca_2Fe_5Si_8O_{22}(OH)_2$	$-31.0 \times 10^6 / (T)^2 + 10^3 / T + 14.9$	Graham et al. (1984)
Serpentine: $Mg_3Si_2O_5(OH)_4$	$27.5 \times 10^6 / (T)^2 - 76.9 \times 10^3 / T + 40.8$	Sakai and Tsutsumi (1978)
Muscovite: $KAl_3Si_3O_{10}(OH)_2$	$-22.1 \times 10^6 / (T)^2 + 10^3 / T + 19.1$	Suzuoki and Epstein (1976)

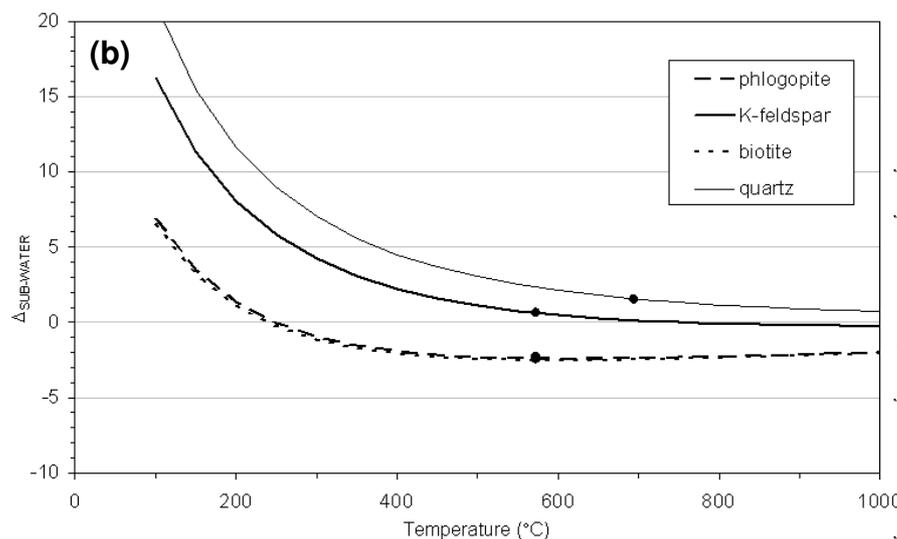Table 7-5 Mineral-SO_4/H_2S fractionation equations for sulphur (Temperature (T) is in Kelvin)

Mineral	Fractionation equation	Reference
Anhydrite: $CaSO_4$	$4-26 \times 10^6 / (T)^2 + 10^3 / T + 6.0$	Ohmoto and Rye (1979)
Pyrite: FeS_2	$0.4 \times 10^6 / (T)^2 + 10^3 / T$	Ohmoto and Rye (1979)
Chalcopyrite: $CuFeS_2$	$-0.05 \times 10^6 / (T)^2 + 10^3 / T$	Ohmoto and Rye (1979)
Covellite: CuS	$-0.4 \times 10^6 / (T)^2 + 10^3 / T$	Ohmoto and Rye (1979)
Sphalerite: ZnS	$0.4 \times 10^6 / (T)^2 + 10^3 / T$	Ohmoto and Rye (1979)
Galena: PbS	$-0.63 \times 10^6 / (T)^2 + 10^3 / T$	Ohmoto and Rye (1979)

_____

Figure 7-2 Fractionation curves for oxygen (a-d), hydrogen (e) and sulphur (f)
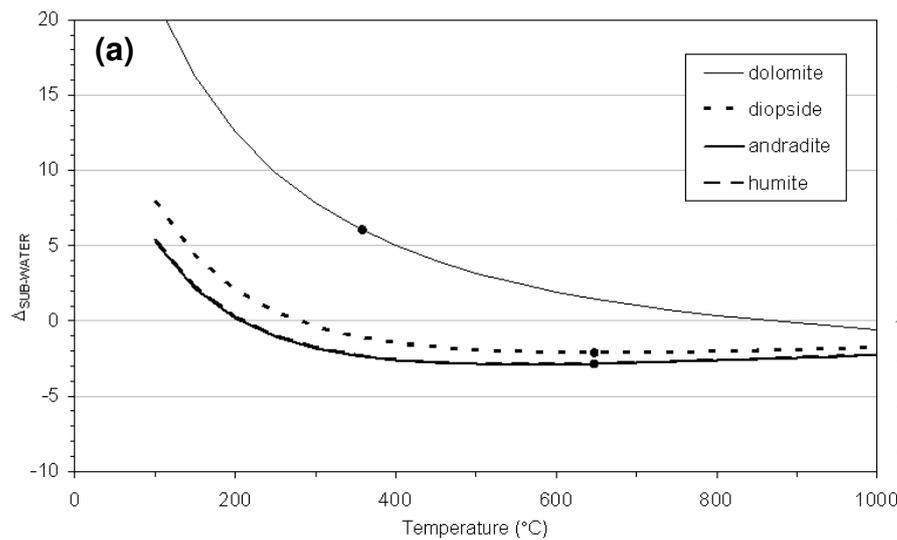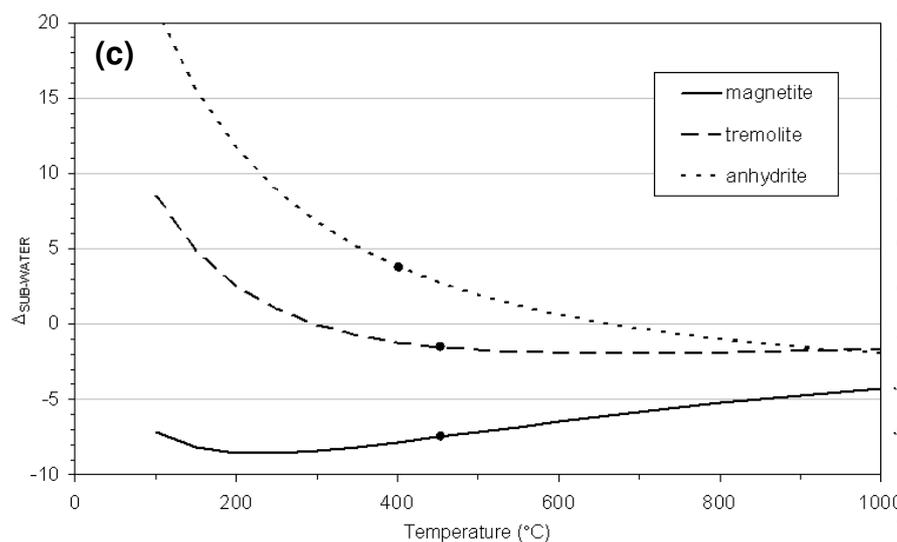

Isotope fractionation curves generated from equations in Table 7-3, Table 7-4 and Table 7-5. (a) (b) (c) (d) oxygen (e) hydrogen (f) sulphur. A dot has been placed on each curve to indicate the temperature that was used to calculate the isotope composition of the fluid for each mineral. The oxygen fraction curves indicate that lower temperatures than those selected will result in higher fractionation values, except for magnetite, while lower temperatures than those selected will result in comparatively lower fractionation values for hydrogen (except serpentine). As the fractionation curves for skarn (a) and potassic (b) minerals have gentle slopes near the temperature selected (dots), the assumed temperatures are considered sound. No data exists for estimating temperature of magnetite formation, however, the fractionation curves are very gentle in the vicinity of the temperature chosen.

Figure 7-2 Fractionation curves for oxygen (a-d), hydrogen (e) and sulphur (f) (cont)
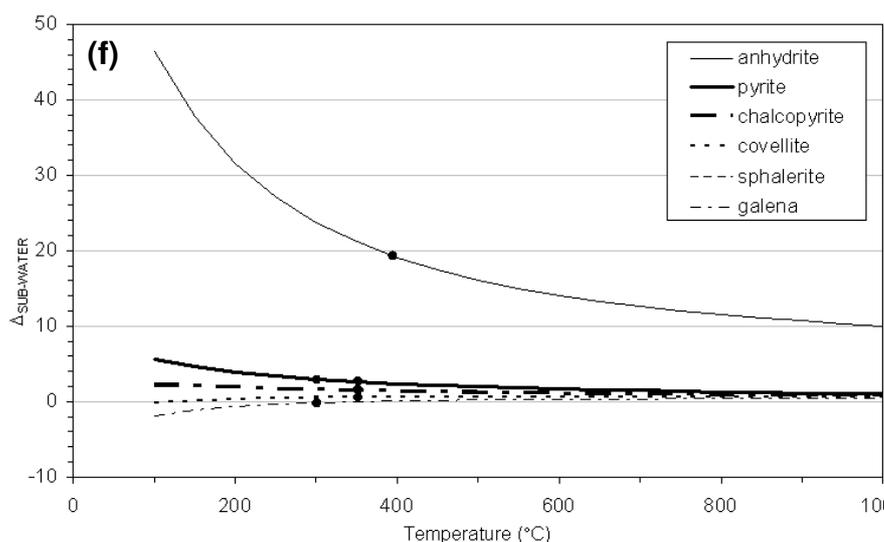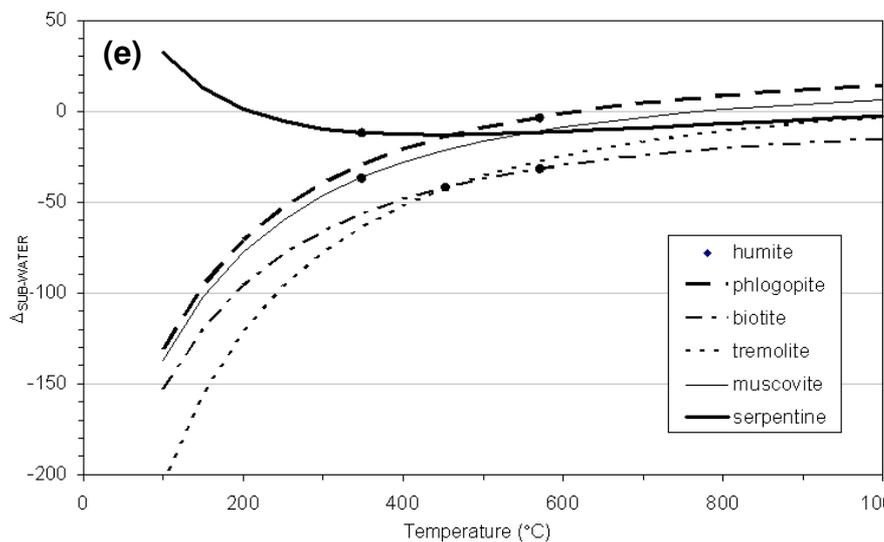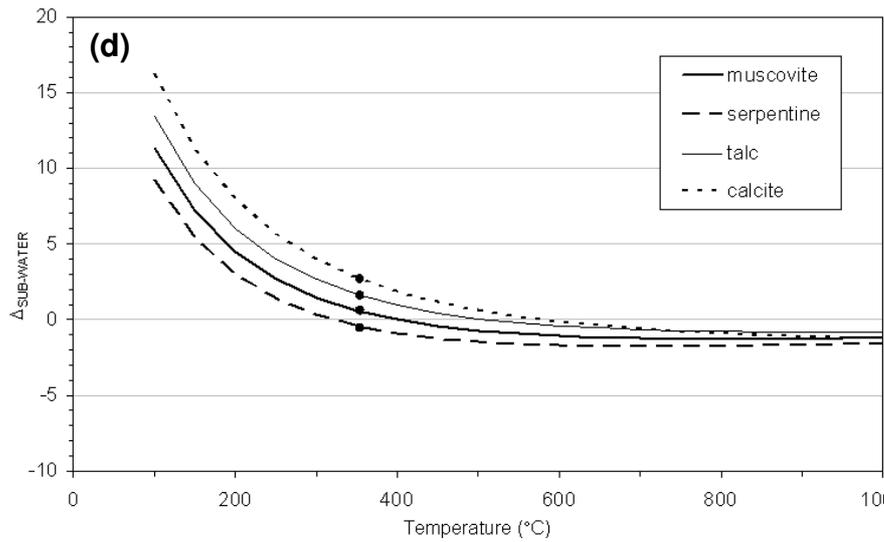
Although tremolite and anhydrite have relatively large slopes the temperatures are thought to be robust (see Discussion) Dolomite and anhydrite may have the greatest temperature uncertainty-related error, as the assumed temperatures used to calculate fluid compositions for these minerals lay along steep sections of their respective fractionation curves. Although the assumed temperatures of minerals in (d) lie on segments of high slope the formation temperatures are constrained by fluid inclusion homogenisation temperatures (Chapter 6) in related quartz alteration. (f) Predicts higher ^{34}S fractionation differences at lower temperatures for anhydrite. As sulphide-fluid fractionations are small the possibility of a large error on calculated fluid composition is also small. Sulphur isotope fractionation is less sensitive to temperature for sulphides than for anhydrite.

_____

Results of fractionation calculations

Estimated $\delta^{18}O_{FLUID}$ displays a positively skewed distribution between 0 and 12‰ with the majority of samples between 4 and 10‰ $\delta^{18}O$ and a maximum at 8-9‰ (Figure 7-3a). Dolomitisation fluids fall outside the main range of fluid compositions, having significantly higher $\delta^{18}O$ of 16-17‰. Group I diopside, garnet, humite and phlogopite plus Group II quartz veins and magnetite formed from fluids with restricted range of $\delta^{18}O$ between 4 and 10‰. Individually, each of these minerals imply $\delta^{18}O_{FLUID}$ values do not vary by more than 2‰. δD of fluid for Group I minerals are preserved in humite and phlogopite which have a large but evenly spread range of values between –225 and –150‰ (Figure 7-3b). Group III biotite and tremolite-actinolite have distinct fluid compositions. While biotite fluid compositions are a single population restricted between 5 and 7‰ $\delta^{18}O$ (Figure 7-3a) and –175 to –150‰ δD (Figure 7-3b), tremolite-actinolite fluids are in two groups of 4-5‰ and 8-10‰ $\delta^{18}O$ (Figure 7-3a). δD_{FLUID} derived from these two minerals range between –175 to –125‰ and –100 to –75‰ δD (Figure 7-3b). Fluids associated with Group III quartz alteration appear to have had a large and continuous variation in $\delta^{18}O$ from 6 to 0‰ (Figure 7-3a). Group III anhydrite precipitated from fluids with $\delta^{18}O$ near 0‰ and $\delta^{34}S$ from –12 to –8‰. Muscovite fluids had $\delta^{18}O$ between 5 and 7‰ and the highest δD recorded for all fluids between –75 and –50‰ (Figure 7-3b). Talc fluids have lower $\delta^{18}O$ between 3 to 4‰ $\delta^{18}O$ (Figure 7-3a). Calculated $\delta^{34}S_{FLUID}$ for pyrite overlaps with those for anhydrite ranging from –10 to –2‰ with a concentration between –8 and –4‰ (Figure 7-3c). $\delta^{34}S_{FLUID}$ values for chalcopyrite and covellite are similar, each having some values close to 0‰ as well as a second group of $\delta^{34}S_{FLUID}$ similar to values for pyrite fluids between –8 and –4‰ (Figure 7-3c). The single samples of sphalerite and galena give comparable values close to 0‰ similar to chalcopyrite and covellite values. Calcite infill that post-dates pyrite alteration and occurs as fracture infill along with high sulphidation nukundamite mineralisation has a calculated $\delta^{18}O_{FLUID}$ between 6 and 7‰ (Figure 7-3a).

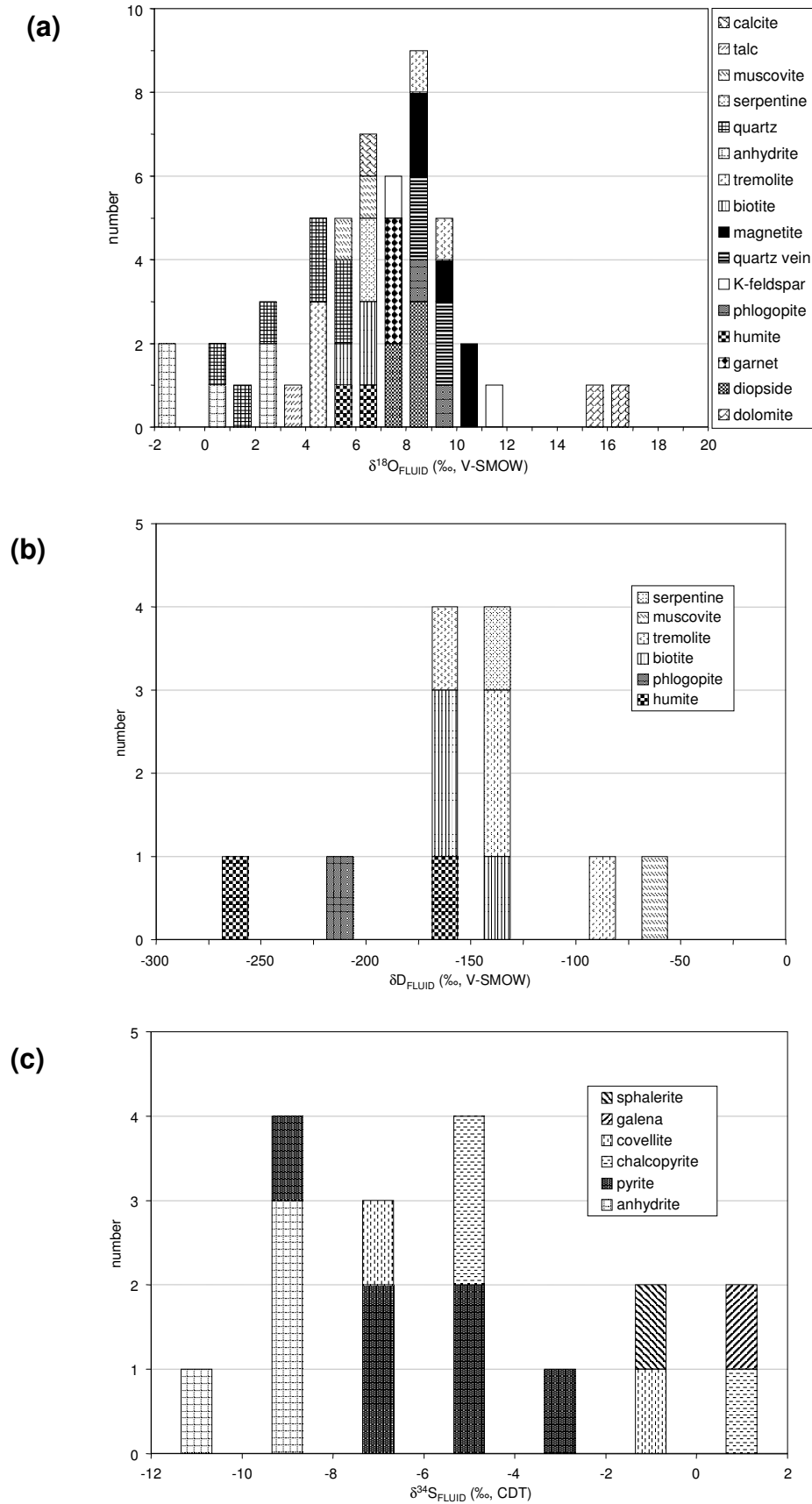Figure 7-3 Histograms showing calculated oxygen, hydrogen and sulphur isotope ratios

_____

7.2 INTERPRETATION

Stable isotopes, in particular oxygen and hydrogen, have been used to constrain the origin of

hydrothermal fluids in Kucing Liar. Oxygen isotope compositions have been used to great effect

in understanding the origin of fluids in geological environments. Restricted ranges of oxygen

compositions for waters derived from deep-sea sediments, limestone, metamorphism and magmas

have been established and are reported as enrichment or depletion in ^{18}O relative to Standard

Mean Ocean Water (SMOW) measured at the equator. However, studies in the North American

continent reveal that isotope fractionation is affected by elevation as well as latitude (Taylor,

1979). As elevation increases, both $\delta^{18}O$ and δD become progressively lower due to fractionation

of oxygen and hydrogen during evaporation and precipitation. As such, data from local snow,

glacial ice and mine water, which indicate values of -125‰ δD and -15‰ $\delta^{18}O$ (Harrison, 2000)

may not be valid for comparison against fossilised hydrothermal systems due to the potentially

dramatic changes in elevation in such an active environment and the potentially large amount of

uplift that has occurred since hydrothermal activity. Local studies at Big Gossan (Meinert *et al.*,

1998) and regional studies of the Southern Ranges (Weiland and Cloos, 1996) have arrived at

comparable figures of 2km for erosion and uplift within the district. The current uplift of 1mm/y

for New Guinea could have produced 3km of uplift in the 3Ma since mineralisation occurred.

This relatively dramatic change in elevation for the Ertsberg Mining District will cause the $\delta^{18}O$

and δD of local meteoric waters at the time of mineralisation to be different from those of

contemporary waters. As such, the local meteoric water compositions at the time of hydrothermal

activity may have been similar to SMOW, and for simplicity in discussion, are treated as such.

Fluid reservoirs and isotopic compositions

The distinct isotopic signature of dolomitisation in Kucing Liar samples matches that of basin

waters, which are expelled from the sediments during orogenesis (*cf*. Hitzman et al., 1997). By

contrast, Group I skarn and Group II potassic fluids all fall within the range of magmatic water.

Quartz and anhydrite from Group III have $\delta^{18}O_{FLUID}$ in part similar to SMOW, ranging up to

compositions of magmatic waters. The systematic variation of isotopic compositions can arise from the gradual mixing of magmatic and local waters (Campbell and Larson, 1998). The progressive shift toward lower values observed in Groups I & II may be the result of minor interaction with meteoric waters, while the oxygen isotope composition of quartz indicates total interaction with a fluid of meteoric water composition. $\delta^{18}O$ values of anhydrite from Group III also indicate derivation of oxygen from fluids with compositions similar to those of standard mean ocean waters (SMOW).

Estimated fluid compositions during the earliest stages of alteration display relatively homogeneous $\delta^{18}O$, and these compositions are shifted significantly from values of $\delta^{18}O$ collected from two samples of dolomitic wall rocks. This would suggest that composition of the wall rocks have no influence of hydrothermal alteration, indicating that the oxygen component of the original carbonate rocks has been completely replaced by the introduced fluid. This is most likely due to high fluid-rock ratios, or in other words that the Kucing Liar is fluid-buffered. Skarn vein material is shifted significantly from that of the sampled dolomite. Three minerals analysed from the skarn group display a progressive decrease with paragenetic time (Figure 7-4). This may indicate some large-scale effect on the fluids by local conditions while the gradual progression in ^{18}O compositions indicates evolution of a common fluid source or mixing with local isotope sources. There is a major change in composition between the composition of calc-magnesian silicate minerals and that of phlogopite alteration, which was assigned to Group I skarn in Chapter 2. The large compositional change is thought to indicate a different fluid source for phlogopite from calc-magnesian skarn. The hydrogen isotope analyses are less exhaustive but display a different relationship in skarn minerals. Two humite samples have very different δD, while a single phlogopite analysis reports a δD value between the two samples of humite.

Sulphur isotopes have also been analysed for anhydrite as well as the primary sulphides and indicate a range from a source depleted in ^{34}S for anhydrite, a source equivalent to primary magmatic sulphur for some of the copper mineralisation, and a source for sulphur that is mixed

_____

between these two end-members. Sulphur isotope data from Kucing Liar are difficult to interpret due to a lack of knowledge concerning details of the fractionation of ^{34}S during fluid evolution and in fluid-rock reactions (*cf.* Ohmoto and Rye, 1979). While the origin of sulphur is elusive, some appreciation can be gained from comparison of data from different minerals. The sulphur in anhydrite is depleted in ^{34}S compared to pyrite, which exhibits a range in compositions, and base metal sulphides have compositions similar to primary magmatic sulphur. As anhydrite is likely to be derived from strongly mixed magmatic-meteoric waters (see above) it is assumed that the depleted ^{34}S values of anhydrite indicate meteoric mixing, leading to an interpretation where the range of pyrite values represents variable mixing between the primary magmatic and non-magmatic sulphur anhydrite.
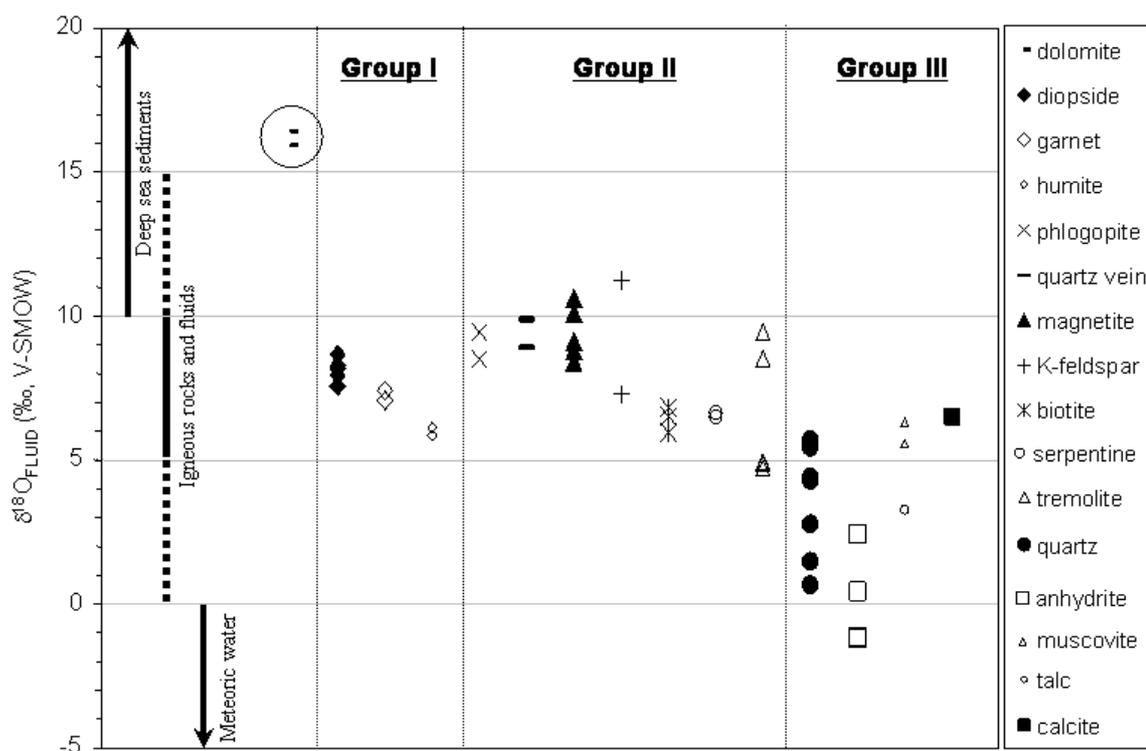

Figure 7-4 Calculated δ^{18}O$_{FLUID}$ for the Kucing Liar paragenesis

Calculated δ^{18}O$_{FLUID}$ arranged in paragenetic sequence illustrate the magmatic affinity of Group I-III as well as their systematic variation. Ranges for fluid reservoirs are from Campbell and Larson (1998).

_____

Magmatic exsolution processes

While oxygen compositions distinguish between ultimate fluid sources, hydrogen isotope compositions can also identify melt-fluid-vapour interactions within the parent magma. As the mass difference between hydrogen and deuterium is 100%, it is the most sensitive to fractionation processes (e.g. Campbell and Larson, 1998) and thus may indicate subtle influence more readily than oxygen isotopes. As deuterium is preferentially fractionated into vapour at high temperatures, a partially degassed magma will be left isotopically lighter in terms of hydrogen (Taylor, 1988). Fluids are either passively exsolved from their magmatic source or are ponded at the upper carapace (Burnham, 1979). Gradual removal of a deuterium-enriched vapour will cause the residual magma and any subsequently derived fluids to have progressively lower δD. However, vapour ponding and catastrophic release will cause the release of fluids with homogenous δD (Taylor, 1988; Taylor, 1997). In this way, magma degassing can account for both clustering (closed system) and large variations (open system) of deuterium compositions due to the preferential fractionation of deuterium into an escaping gas phase (Talyor, 1988; Hedenquist and Richards, 1998). Open system degassing can produce deuterium depletions down to $-140‰$ for small water fractions, which has been corroborated by observations of natural systems where there is direct correlation between low δD and low remaining fractions of wt% H_2O as determined from gas trapped in lava (Taylor, 1988).

Hydrogen isotope analyses conducted on a small group of samples indicates that magnesian skarn, represented by humite and green phlogopite, formed from fluids with variable but consistently very low δD values. By contrast, Group II biotite fluids, although still much lower than primary magmatic waters are tightly clustered about -150‰. Tremolite-actinolite fluids also have a large range in δD values that are lower than primary magmatic waters, whereas these minerals suggest little variation in $\delta^{18}O_{FLUID}$. The development of very low δD values in hydrothermal minerals may result from degassing of magma prior to fluid exsolution. The trend of increasing δD with time for Kucing Liar fluids is opposite to what is expected to result from continued exsolution of

_____

a finite water source from magma chamber. This could indicate mixing with isotopically "heavier" local meteoric waters, or replenishment of the source area with new magma influxes, which would "reset" the δD values for new fluid fractions. If this were the case, replenishment would have had to have occurred prior to potassic alteration and again prior to phyllic alteration.
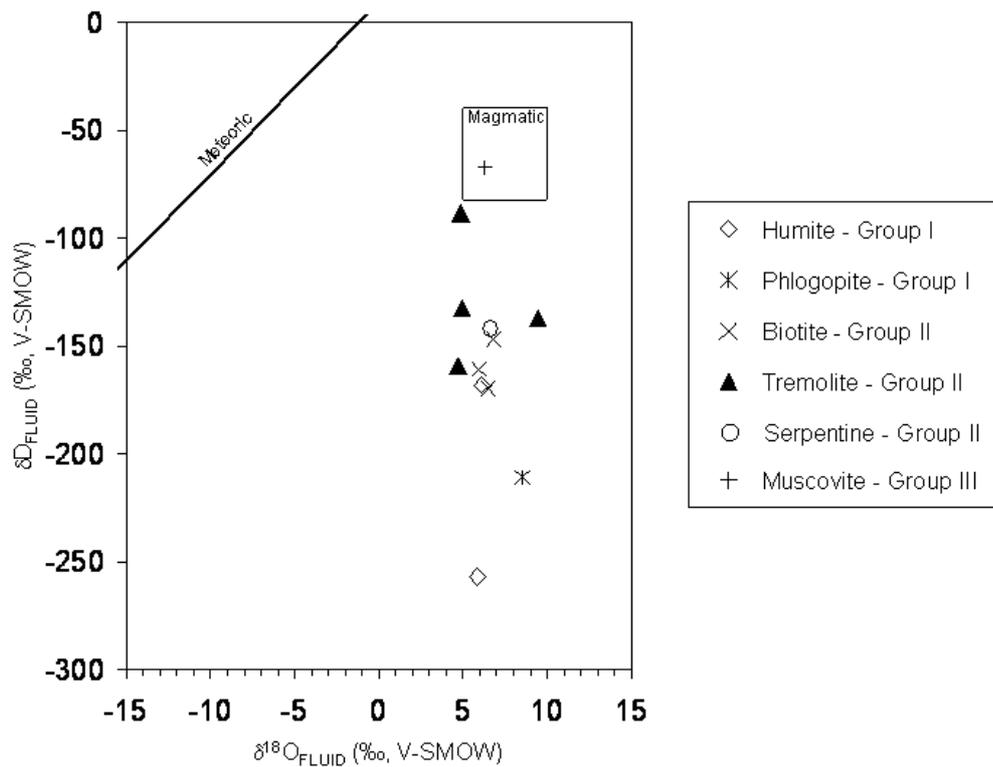

Figure 7-5 Calculated Hydrogen and oxygen isotope compositions of Kucing Liar fluids
Magmatic box based on Campbell and Larson (1998) and meteoric water line from Craig (1961).

8 $^{40}Ar/^{39}Ar$ geochronology

The primary geochronological tool used was ^{40}Ar-^{39}Ar dating, providing a much higher degree of precision than K-Ar published dates in the Ertsberg Mining District. Re-Os dates of molybdenite are also presented. These methods are reported to be comparable in terms of accuracy and high precision (Richards and Noble, 1998). It has been suggested that Re-Os dating techniques are more reliable than other dating techniques as it is not susceptible to resetting due to thermal disturbances post-formation, and that, together with ^{40}Ar-^{39}Ar, provides the most accurate ages for mineralisation (Stein *et al.*, 1997). The use of Re-Os has been found to be reproducible and able to give an age for mineralisation even in disturbed terranes (Watanabe and Stein, 2000). Two green phlogopite samples, three biotite samples and two muscovite samples of pure mineral material were despatched to Lisa Peters at the New Mexico Geochronology Research Laboratory (NMGRL) and a single sample containing molybdenite was delivered to Ryan Mathur at the University of Arizona for Re-Os analyses. Details of the analytical procedures followed by each laboratory are included in Appendix VIII. Minerals suitable for $^{40}Ar/^{39}Ar$ geochronometry are restricted to phases containing >0.3wt% K_2O content and were chosen to represent two separate groups of paragenetic assemblages; green phlogopite and biotite represent latest skarn and potassic alteration while muscovite represents the Group III assemblage. Samples of pure mineral were generated by hand picking grains and clusters of grains from pulverised rock sample after splitting to 250µm size fractions. Green phlogopite places a maximum age constraint for potassic alteration and a minimum age for skarn development, while biotite is considered to place minimum age constraints on potassic alteration. Together, these two micas should reveal the time-scale for potassic alteration. Muscovite provides a minimum age of quartz alteration and a maximum age for covellite-bearing mineralization. Molybdenite is expected to place a minimum age on covellite-bearing high sulphidation mineralizaton as it overprinted covellite (Chapter 3).

_____

8.1 SAMPLE COLLECTION

Mineralogical and textural/relative timing descriptions plus a photograph (Figure 8-1 & Figure 8-2) is provided for each sample from which pure mineral separates were collected. The samples in paragenetic order are:

- KL28-1 360.3m, composed of very coarse-grained green phlogopite, vein K-feldspar, magnetite fracture infill and chalcopyrite alteration/infill spots (Figure 8-2a). The phlogopite that was extracted is penetrative alteration of an unknown precursor and is restricted to a 5m drill intersection that marks a spatial transition from a K-feldspar-quartz-muscovite-pyrite-covellite-native sulphur assemblage to intense magnetite-pyrite-chalcopyrite replacement of unknown lithology and is interpreted to be within a fault zone (see Chapter 3). Petrographically this phlogopite has pale green pleochroism.

- KL32-8 331.0m, composed of strongly fragmented humite-phlogopite-chrysotile-anhydrite-gypsum-serpentine rock (Figure 8-2b). The phlogopite separated consisted of coarse, very pale green to almost colourless idiomorphic grains associated with the fragment of humite-altered rock. Pyrite-chalcopyrite mineralisation is associated with a band of anhydrite-gypsum and is crosscut by serpentine. Petrographically the phlogopite has pale green pleochroism.

- KL32-5 539.6m, composed of coarse-grained red-brown biotite-tremolite-talc-pyrite-chalcopyrite in which the biotite has cross-cut tremolite as centimetre scale selvage alteration (Figure 8-2e). Petrographically the biotite has very pale brown pleochroism and similar transparency to the green phlogopite samples collected from KL28-1 360.3m and KL32-8 331.0m. The sample is from a discrete 5m-scale zone of coarse-grained biotite-tremolite-anhydrite within a 10m-scale zone of magnetite-pyrite-chalcopyrite alteration. Together these are interpreted to represent a fault zone which separates fine-grained K-feldspar-muscovite-pyrite-covellite altered sandstone from clinopyroxene-humite-tremolite-anhydrite altered limestone (see Chapter 3).

_____

- KL32-5 652.4m, composed of penetrative K-feldspar and fine and coarse-grained biotite alteration and fracture infill and quartz infill (Figure 8-2c). Petrographically the biotite has dark orange pleochroism. Pure biotite was collected from infill that lines a fracture later infilled with quartz and from intense alteration directly adjacent to the fracture. The sample originates from displaced sections of the upper Waripi shale marker (see Chapter 3) in the footwall of the Idenberg fault zone.

- KL20-9 465.3m, composed of clinopyroxene-feldspar alteration overprinted successively by quartz veins, magnetite fracture infill and anhydrite alteration. Coarse-grained biotite is associated with the quartz veins (Figure 8-2d). Petrographically the biotite has dark orange pleochroism. It is unclear if the biotite in this sample has overprinted the quartz vein in a crosscutting fracture or if it is wall rock included at the margin of the vein. In the former case it would represent the only identified example of biotite infill in a quartz vein, though there are few examples of definitive relationships between quartz and biotite (see Figure 8-2c). The sample is derived from the lower Ekmai limestone (see Chapter 3).

- Sample KL32-8 455.9m, a rock affected by semi-penetrative fine to medium-grained muscovite alteration (plus vugh infill) of penetrative K-feldspar alteration (Figure 8-2f). Petrographically the muscovite forms clusters of coarse-grains in vughs and fine-grained accumulations in zones where the underlying K-feldspar can still be identified. The sample also contains vein and fracture selvage alteration comprising anhydrite-pyrite-nukundamite-chalcocite (Figure 8-2f). The sample is collected from the centre of a quartz-muscovite-pyrite alteration zone localised about the Waripi limestone-Ekmai limestone contact (see Chapter 3).

- Sample KL32-1 255.7m is fine-grained muscovite infill that has grown in millimetre-scale cavities in quartz-altered rock (Figure 8-2g). The muscovite is very fine-grained and the cavities are lined with quartz crystals that protrude inwards (Figure 8-1). Elsewhere, similar vughs are infilled with fluorite-pyrite-covellite. The sample is from a thick section of quartz-

_____

pyrite-muscovite altered drill core at the very top of the mineralised zone that is interpreted to be in the centre of the Idenberg fault zone (see Chapter 3).

- Sample KL42-2 440.5m contains intensely coarse-grained molybdenite mineralisation in K-feldspar-quartz-pyrite alteration (Figure 8-2h). Covellite occurs in the molybdenite clumps and is interpreted to predate the molybdenite. The sample was collected from a K-feldspar-quartz alteration sandwiched between zones of 10m-scale penetrative pyrite alteration that overprinted locally intense magnetite. Although petrological examination was indeterminate concerning the relative timing of covellite and molybdenite, petrographic textures illustrated in Chapter 3 suggest that some molybdenite formed after covellite.
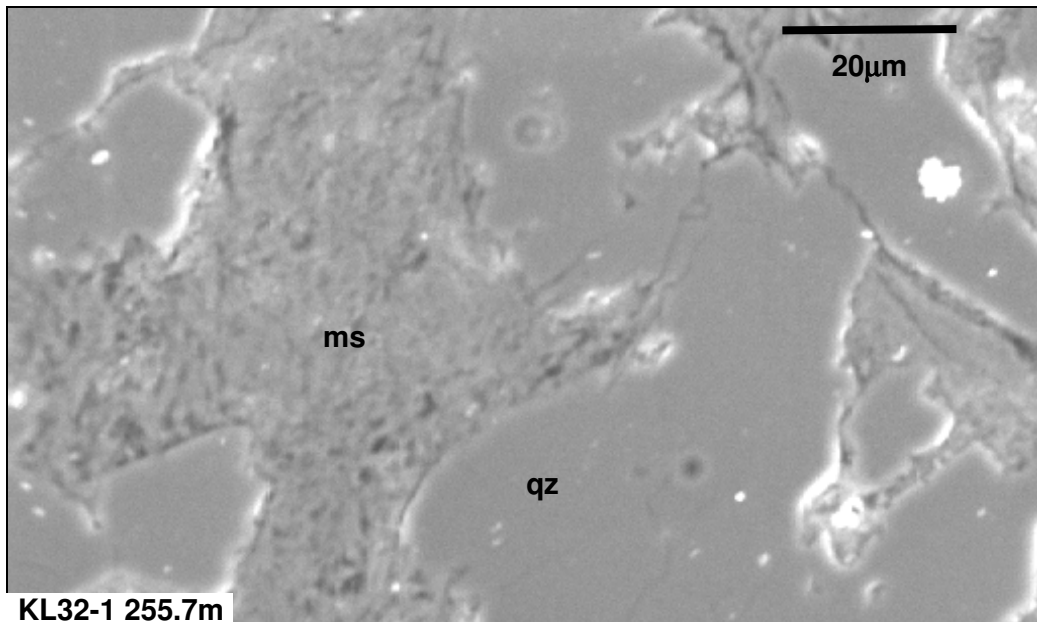
Figure 8-1 Grainsize of muscovite crystals

An SEM image illustrating a cavity surrounded by Group IV quartz alteration infilled with very fine-grained muscovite. The grains of muscovite are only 5-10μm in length, which is at the borderline of acceptable grainsize for the $^{40}Ar/^{39}Ar$ method.
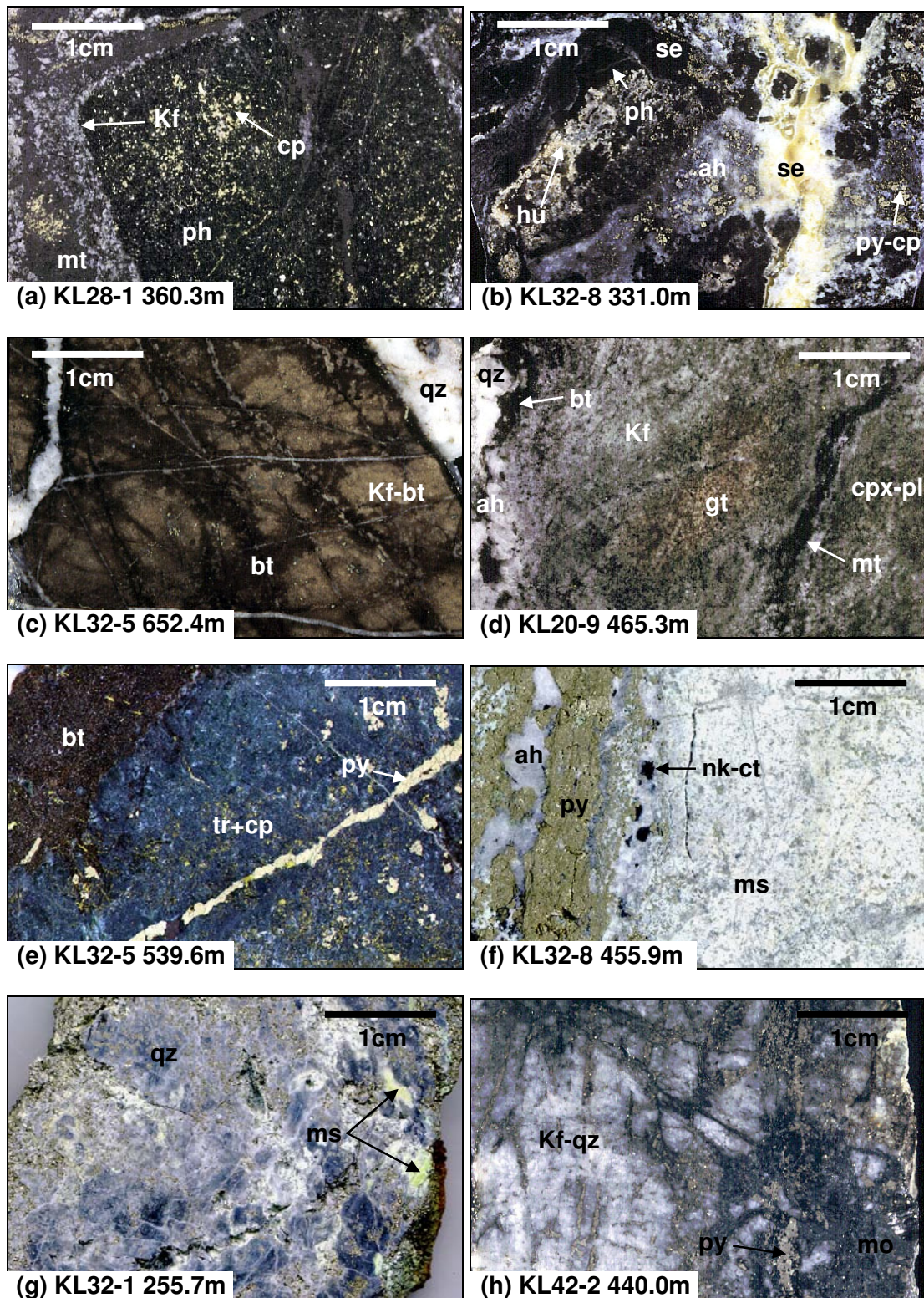
Figure 8-2 Photographs of geochronology samples

(a) & (b) Samples from which pure green phlogopite was extracted for Group I age. (c) (d) & (e) Samples from which pure biotite was extracted for Group II age. (f) & (g) Samples from which pure muscovite was extracted for Group II age (h) Sample from which pure molybdenite was extracted for Re-Os analysis to determine youngest possible age for hydrothermal activity.

_____

8.2 AGE SPECTRA AND RESULTS FROM ANALYSES

The ages established from the results of high precision $^{40}Ar/^{39}Ar$ and Re-Os geochronology conducted on alteration minerals are recorded in Table 8-1 and Figure 8-10. All samples except KL28-1 360.3m (green phlogopite) were analysed in the same sample run. $^{40}Ar/^{39}Ar$ ages are determined from a plateau or an isochron. A plateau age is defined as the age of contiguous temperature steps whose individual ages overlap within experimental error and whose cumulative $^{39}Ar_K$ comprises greater than 50% of the total $^{39}Ar_K$ released from the sample (Snee et al., 1988). The results of step heating are presented as age spectra and isochrons in Figure 8-3 to Figure 8-9 and detailed analyses of the results as reported by the laboratory are included in Appendix VIII.

The ages of green phlogopite samples overlap with one biotite sample. Green phlogopite samples have similar ages with broadly overlapping uncertainties that define a large time period totalling 180ka between 3.42 ± 0.04Ma and 3.34 ± 0.07Ma (Table 8-1, Figure 8-10). By contrast, two samples of biotite collected from infill, KL32-5 652.4m and KL20-9 465.3m, have nearly identical ages and age uncertainties recording a total age range for their formation of only 80ka between 3.2 ± 0.04Ma and 3.18 ± 0.02Ma (Table 8-1). Biotite collected from selvedge alteration in sample KL32-5 539.6m has an age of 3.28 ± 0.04Ma which overlaps with both the older green phlogopite and the younger biotite infill. While the mica crystals in this sample are brown-coloured, they are more similar petrographically to the green phlogopite than the biotite infill samples. The two samples of muscovite returned very different ages. Sample KL32-8 455.9m records an age of 3.18 ± 0.02 contemporaneous with biotite infill, while sample KL32-1 255.7m from the uppermost section of the Idenberg fault zone records an age of 3.45 ± 0.06, which is contemporaneous with green phlogopite (Table 8-1). This age is problematical as textural evidence indicates significant episodes of mineral development occurred between green phlogopite and muscovite.
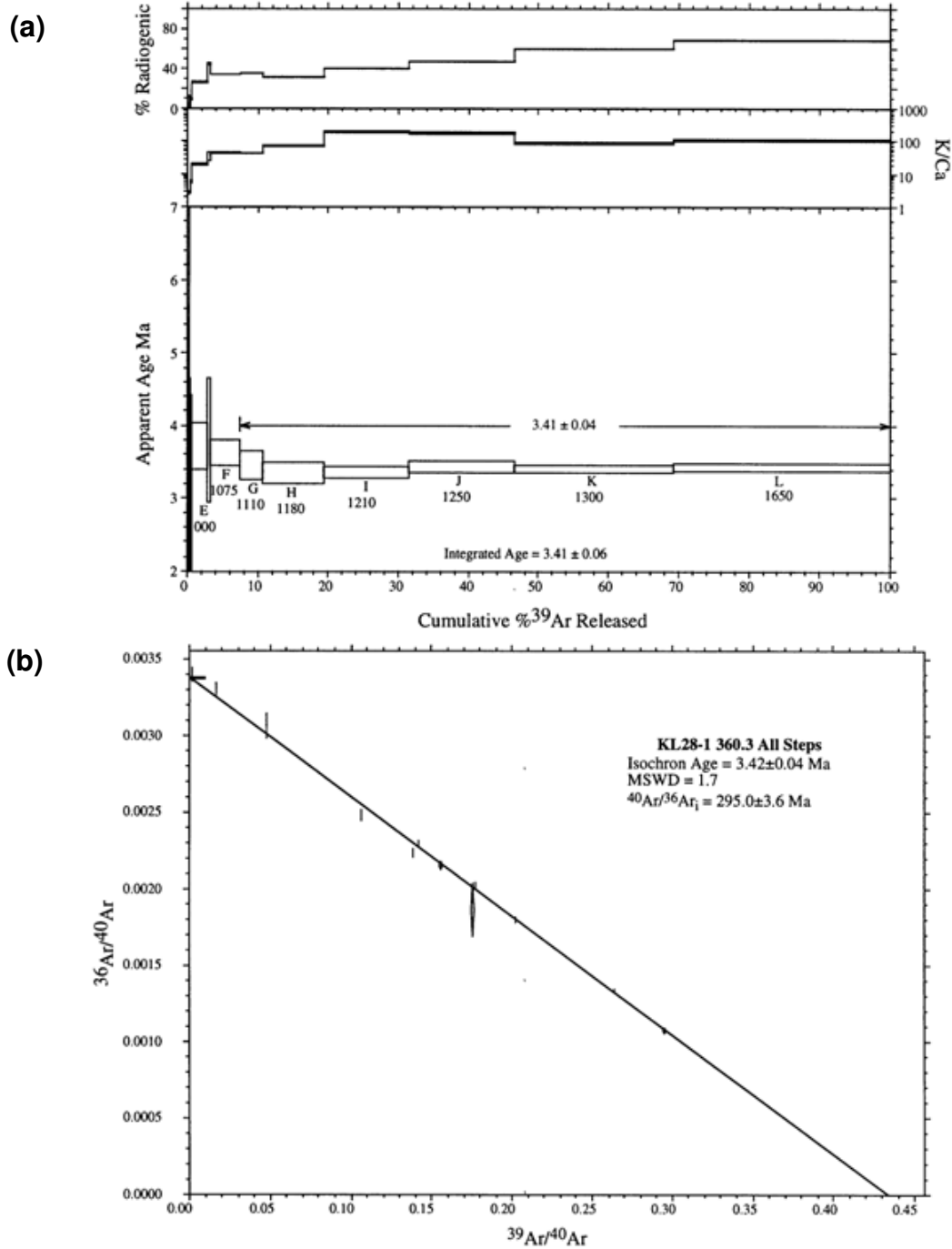
_____

(a)

(b)

Figure 8-3 Age spectra and isochron plots of sample KL28-1 360.3m (green phlogopite)

The slight downward curve of steps E-H is suggestive of excess ^{40}Ar. This sample was part of a different study and this plot was provided by Pollard (pers comm.) after material initially supplied by Peters (pers comm.).
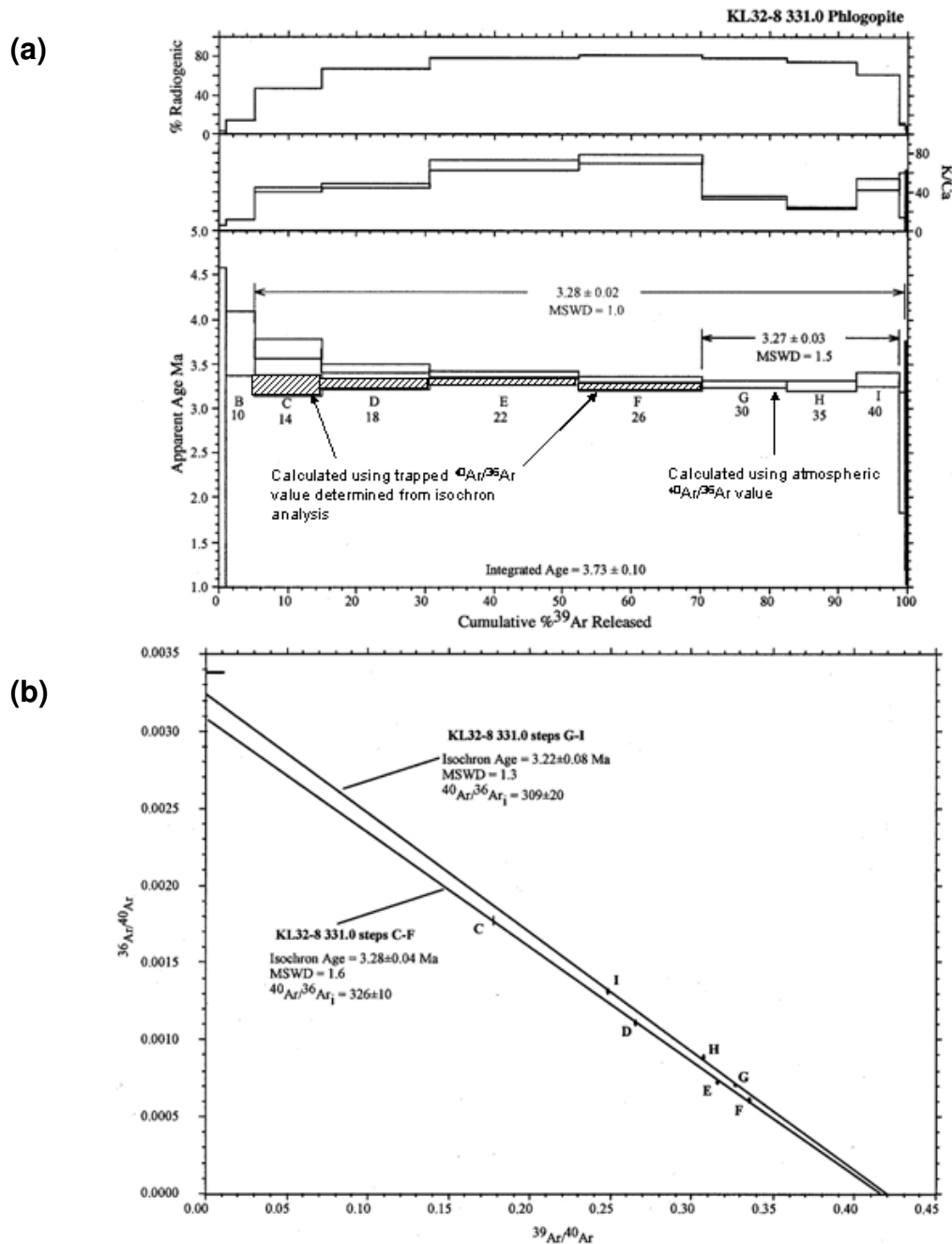
Figure 8-4 Age spectra and isochron plots of sample KL32-8 331.0m (green phlogopite)

The first ~70% of the age spectrum (a) from sample KL32-8 331.0m phlogopite displays decreasing apparent ages correlated with increasing radiogenic yields. A weighted mean age of 3.27 ± 0.03Ma with an acceptable MSWD is calculated from the remaining portion of the age spectrum. Inverse isochron analysis (b) of this sample reveals two trapped components (Heizler and Harrison, 1988). Steps C-F reveal an age of 3.28 ± 0.04Ma with a $^{40}Ar/^{36}Ar$ intercept of 326 ± 10 and an acceptable MSWD of 1.3. Steps C-F, calculated using the $^{40}Ar/^{36}Ar$ ratio indicated by the inverse isochron analysis rather than the atmospheric value that is normally used for age spectrum analysis, are shown plotted with cross hatching on the spectrum diagram. A weighted mean age of 3.28 ± 0.02Ma is calculated from steps C-F of the isochron analysis and steps G-I of the age spectrum analysis. Figure and discussion reproduced from Peters (pers comm.) (see Appendix VIII).
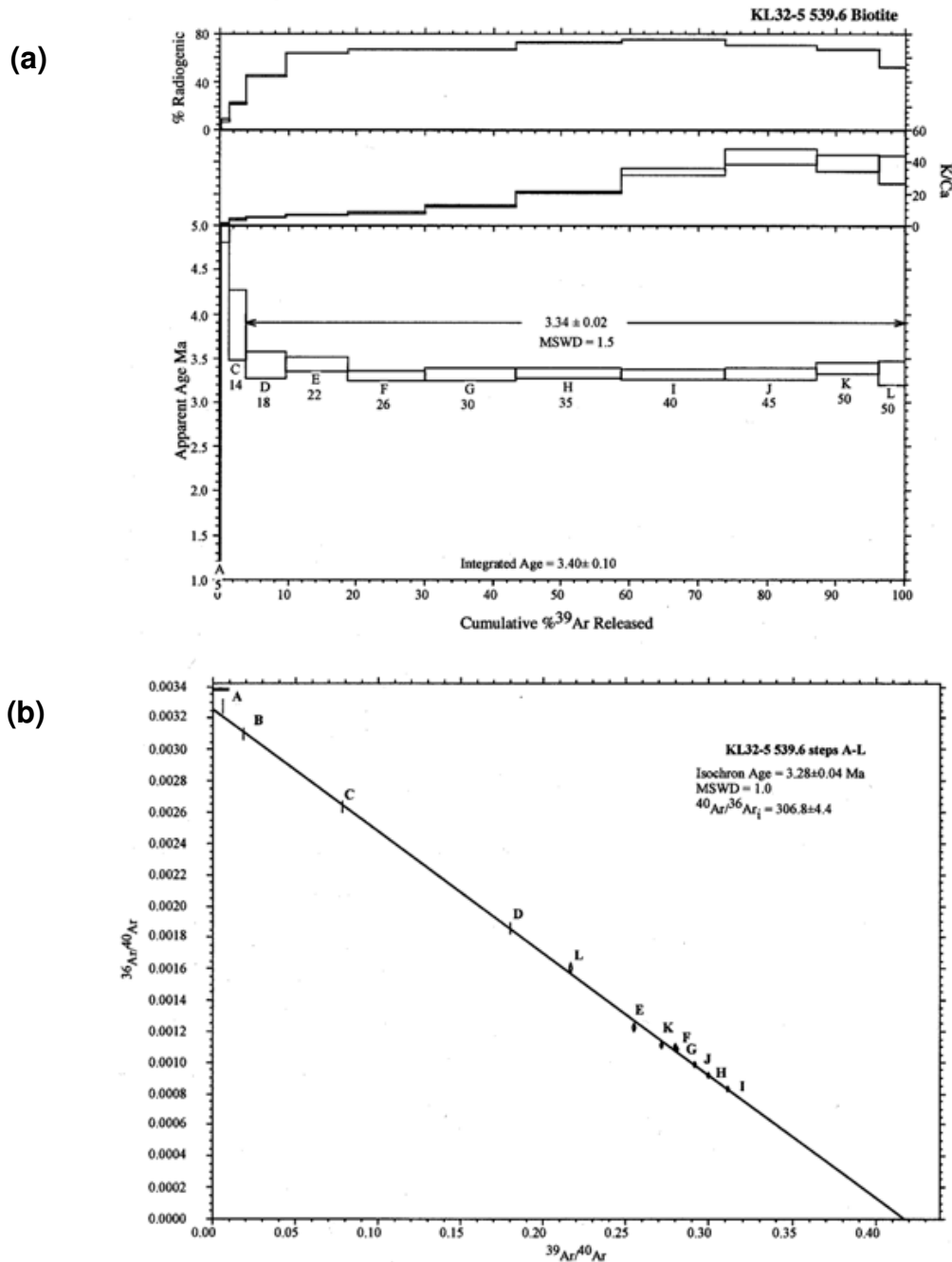
Figure 8-5 Age spectra and isochron plots of sample KL32-5 539.6m (brown biotite)

The slight downward curve of steps C-E (a) is suggestive of excess ^{40}Ar. After the first ~4% of the ^{39}Ar released, the age spectrum from phlogopite sample KL32-5 539.6m is concordant and yields a weighted mean age of 3.34 $\pm$ 0.02Ma with and acceptable MSWD of 1.5 (cf. Mahon, 1996). Inverse isochron analysis (b) of this sample reveals a ^{40}Ar/^{36}Ar intercept (306.8 $\pm$ 4.4) above the atmospheric intercept of 295.5. The isochron age of 3.28 $\pm$ 0.04Ma also has an acceptable MSWD of 1.0. The old apparent ages in the first 10% of the ^{36}Ar released correlates with an increase in radiogenic yield, a pattern often seen in samples that contain excess argon (trapped component greater than atmospheric ^{40}Ar/^{36}Ar ratio of 295.5). Figure and discussion reproduced from Peters (pers comm.) (see Appendix VIII).
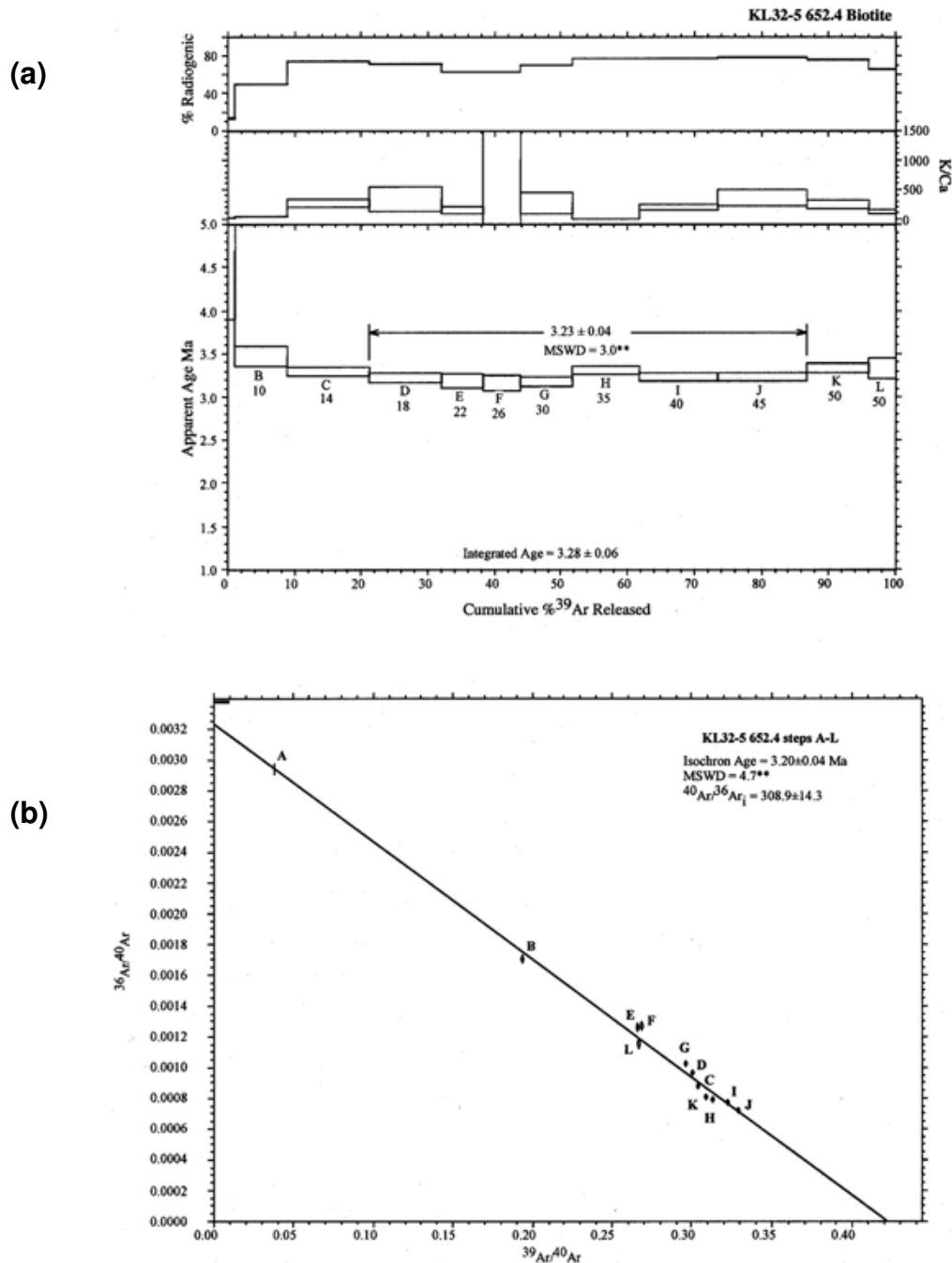
Figure 8-6 Age spectra and isochron plots of sample KL32-5 652.4m (brown biotite)

The first 10-20% of the ^{39}Ar released from phlogopite sample KL32-5 652.4m yields old apparent ages and the remainder of the age spectrum is relatively flat (a). A weighted mean age calculated from steps D-J (3.23 ± 0.04Ma) has an MSWD value of 3.0, slightly above the acceptable value. When plotted on an inverse isochron (b), an age of 3.20 ± 0.04Ma is revealed with a ^{40}Ar/^{36}Ar intercept of 308.9 ± 14.3. Figure and discussion reproduced from Peters (pers comm.) (see Appendix VIII).
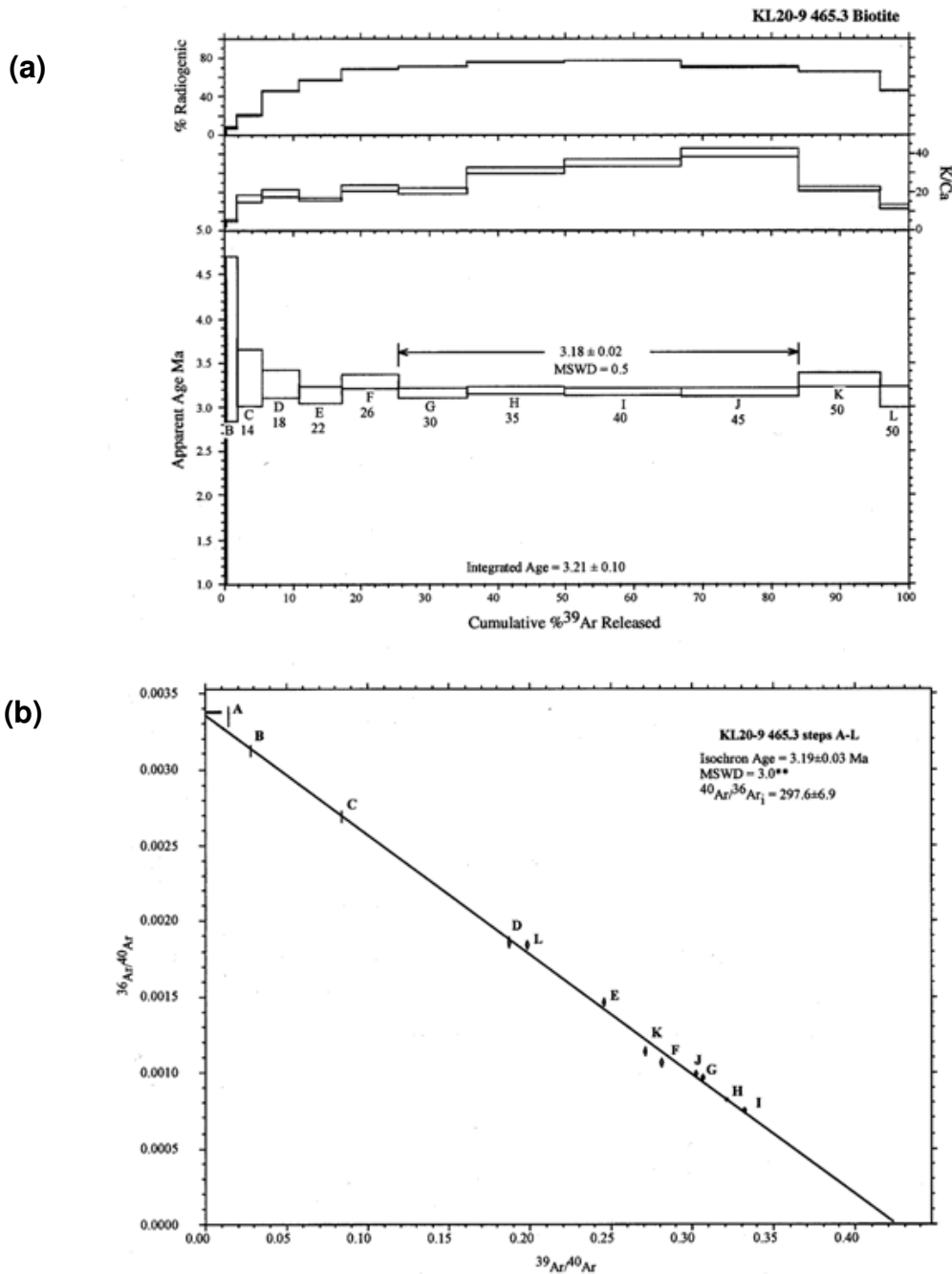
Figure 8-7 Age spectra and isochron plots of sample KL32-5 465.3m (brown biotite)

Phlogopite from sample KL20-9 465.3m yields a nearly concordant age spectrum (a). A weighted mean age of 3.18 ± 0.02Ma with an acceptable MSWD is calculated for steps G-J. Inverse isochron analysis (b) of steps A-L yields an isochron age of 3.19 ± 0.03Ma with a $^{40}Ar/^{36}Ar$ intercept (297.6 ± 6.9) that agrees within error to the atmospheric ratio. Figure and discussion reproduced from Peters (pers comm.) (see Appendix VIII).
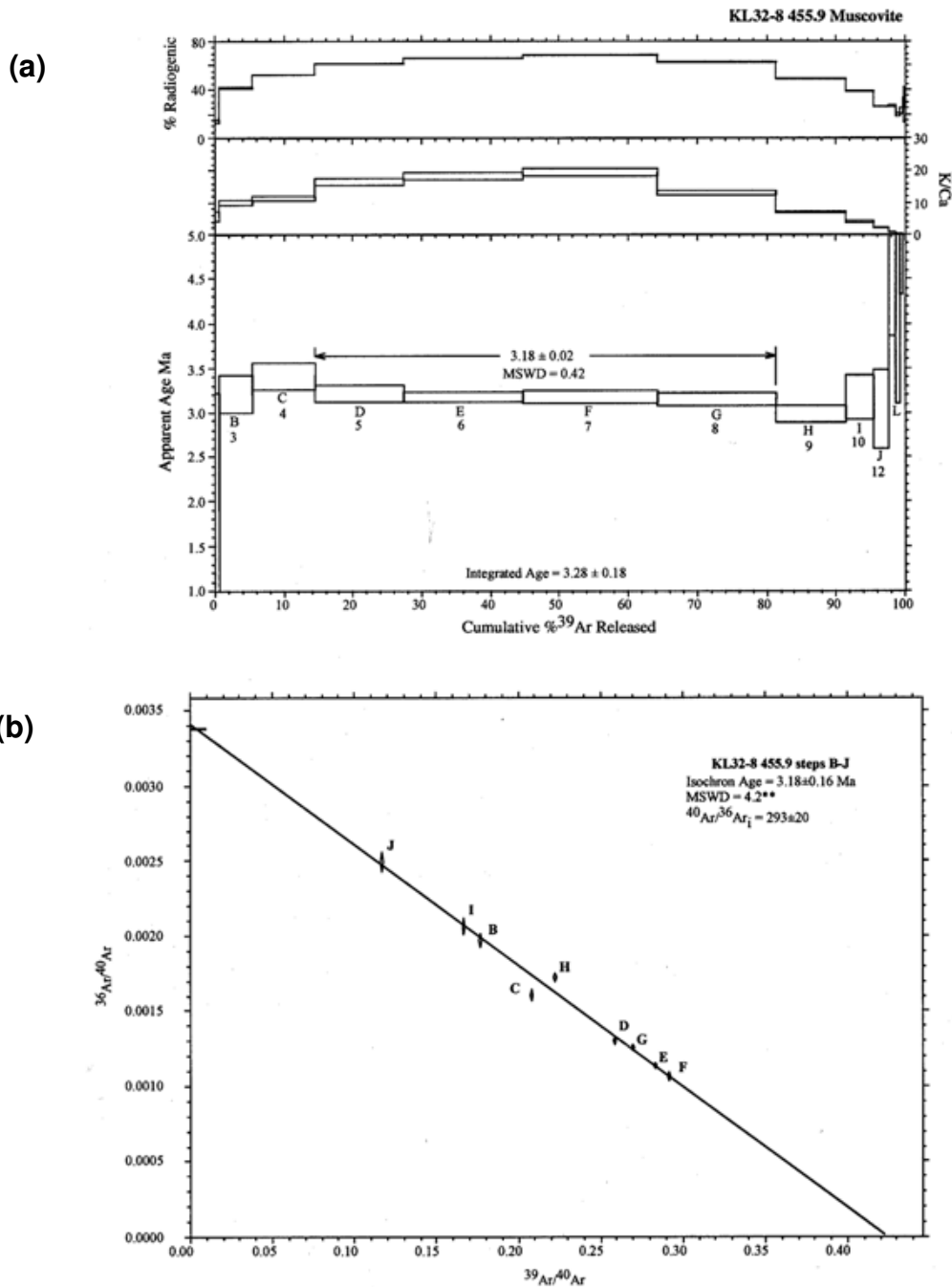
Figure 8-8 Age spectra and isochron plots of sample KL32-8 455.9m (muscovite)

Muscovite from sample KL32-8 455.9m yields a nearly flat age spectrum (a). A weighted mean age of 3.18 ± 0.02Ma calculated from heating steps D-G contains ~67% of the ^{39}Ar released and has an acceptable MSWD. The rise in apparent ages displayed in the last ~10% of the age spectrum correlated with a drop in both K/Ca and radiogenic yield is probably due to high Ca inclusions such as sphene or apatite. An inverse isochron (b) of steps B-J reveals an apparent age of 3.18 ± 0.16Ma with an ^{40}Ar/^{36}Ar intercept (293 ± 20) that agrees within error to the atmospheric ratio and has an acceptable MSWD value of 4.2. Figure and discussion reproduced from Peters (pers comm.) (see Appendix VIII).
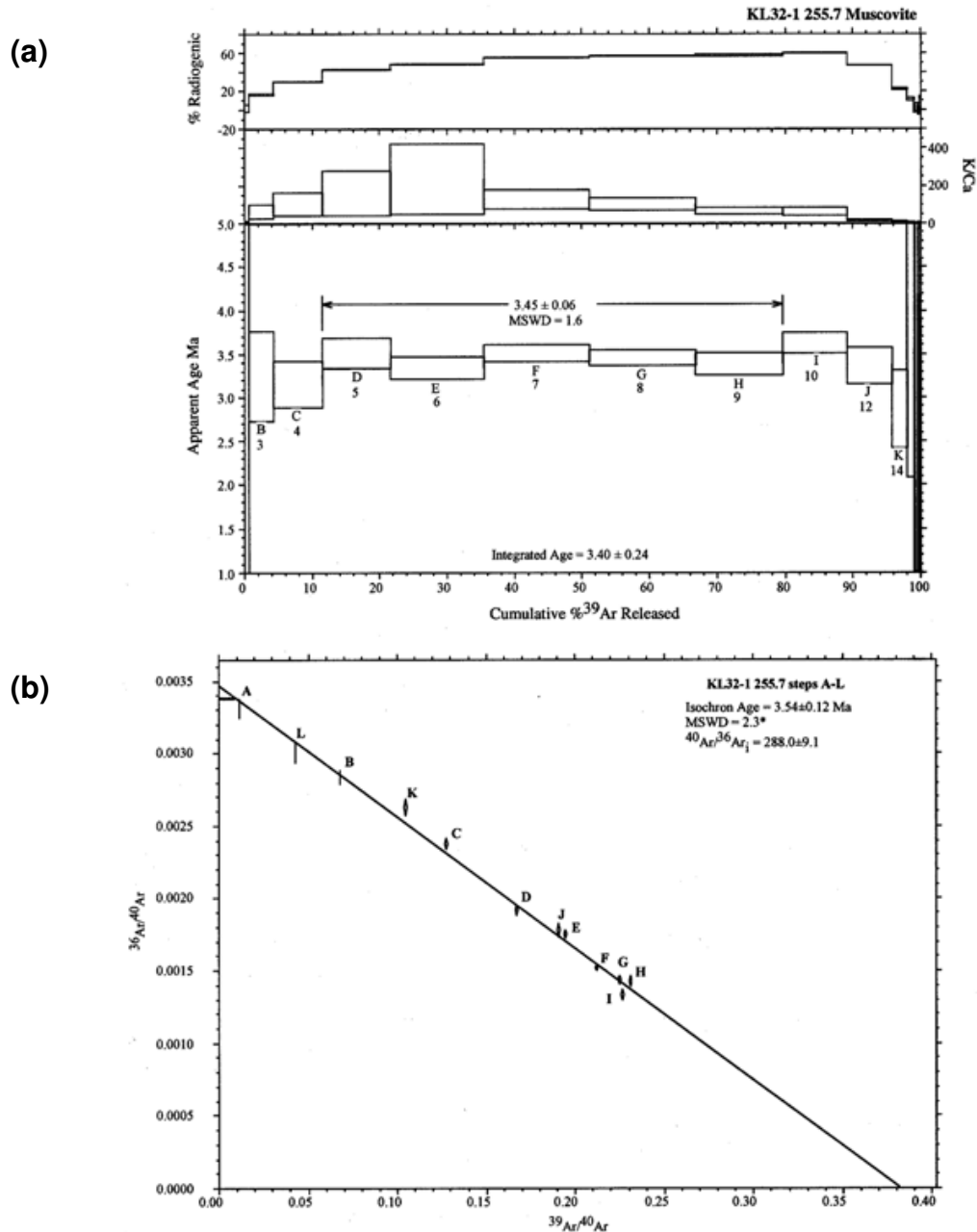
(a)

(b)

Figure 8-9 Age spectra and isochron plots of sample KL32-1 255.7m (muscovite)

The slight downward curve of steps E-H is suggestive of excess ^{40}Ar. Muscovite from sample KL32-1 255.7m yields a slightly hump-shaped age spectrum. A weighted mean age of 3.45 ± 0.06Ma with an acceptable MSWD value is calculated for heating steps D-H. The inverse isochron reveals an ^{40}Ar/^{36}Ar intercept (288.1 ± 9.1) that agrees within error to atmosphere.

_____

Table 8-1 Ages and precisions for ^{40}Ar/^{39}Ar methods on selected minerals

Sample	Mineral	Lithology	Age (Ma)	MSWD	error (Ma)	Age (Ma)	error (Ma)	MSWD
			Plateau			Isochron		
KL28-1 360.3m	Phlogopite	Fault	3.41		0.04	3.42*	0.04	1.7
KL32-8 331.0m	Phlogopite	Limestone	3.27	1.5	0.03	3.28	0.04	1.6
KL32-5 539.6m	Biotite	Fault	3.34	1.5	0.02	3.28*	0.04	1.0
KL32-5 652.4m	Biotite	Shale	3.23	3.0	0.04	3.20*	0.04	4.7
KL20-9 465.3m	Biotite	Shale	3.18*	0.5	0.02	3.19	0.03	3.0
KL32-8 455.9m	Muscovite	Shale	3.18*	0.42	0.02	3.18	0.16	4.2
KL32-1 255.7m	Muscovite	Fault	3.45*	1.6	0.06	3.54	0.12	2.3

Both plateau and isochron age dates are shown for each mineral for comparative purposes. The age attributed to each sample by Peters (pers comm.) has been marked by an asterisk (see caption discussions of Figure 8-3 to Figure 8-9). Note that only sample KL32-8 331.0m does not have good agreement between plateau and isochron ages. As such Peters (pers comm.) has attributed a weighted mean age of 3.28 ± 0.02Ma to this sample (see Figure 8-4 and Appendix VIII).
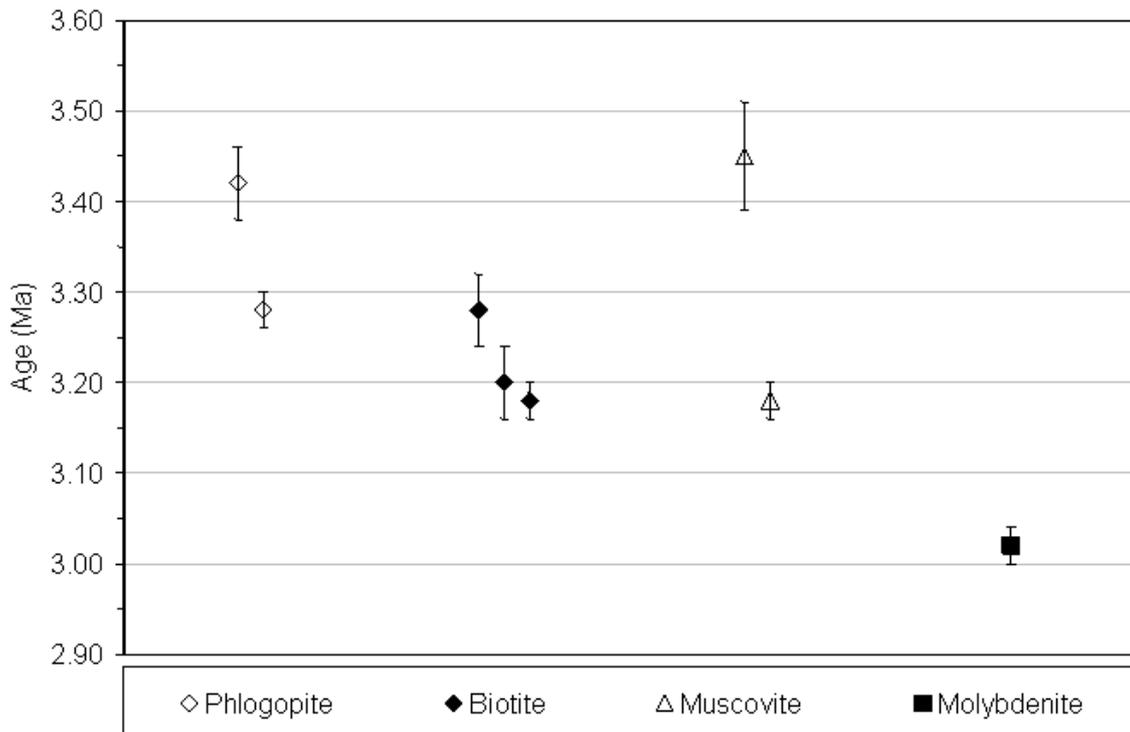

Figure 8-10 Absolute ages of hydrothermal minerals and their accuracies

Mineral phases are grouped into paragenetic sub-stages and placed in order from left to right.

_____

8.3 INTERPRETATION OF AGE DATA

Geochronology has been used to confirm and calibrate the relative sequence of minerals established from visual examination.

Interpretation of Kucing Liar age data

^{40}Ar/^{39}Ar ages in general represent the time when argon exchange between mineral and surrounding rock ceased. As such, this time may represent either:

1. crystallisation

2. resetting of the potassium-argon system by some event after mineral formation

3. closure to argon diffusion after slow cooling from crystallisation temperature to closure temperature (Snee et al., 1988).

The spectra recorded from results of this study all appear undisturbed and do not record any significant overprinting, resetting or disturbances in the argon gas emissions (e.g. Richards and Noble, 1998) from the sample, though several samples have small indications of excess ^{40}Ar (see Appendix VIII). Hence, the ages reported for Kucing Liar samples are interpreted to represent the age of crystallisation of the mineral as there is no disruption of the age spectra and, the shallow depth of the Kucing Liar system would not be conducive to slow cooling which precludes any of the ages being a closure age for argon diffusion (closure temperatures for argon diffusion are reported as 300-350°C for biotite (significantly higher for phlogopite) and 350-400°C for muscovite (Peters, 2001)). While the results derived from ^{40}Ar/^{39}Ar geochronology indicate that analyses represent ages of crystallisation, the tendency for older ages to have lower precision could indicate an extended period where the temperature was greater than the closure temperature. The large disparity in ages for muscovite is thought to be a function of grainsize, which may cause recoil due to very fine grainsize (Richards and Noble, 1998), supported by the apparent influence of excess ^{40}Ar (Appendix VIII). The problematical muscovite age derived from sample

_____

KL32-1 255.7m (Figure 8-1) may be unreliable, as anomalously old ages have been reportedly

derived from samples that have very fine grainsize of 5-10μm (Richards and Noble, 1998).

It is not known when skarn alteration began. The two green phlogopite samples have two very

different ages of 3.42 ± 0.04Ma and 3.28 ± 0.02Ma (Table 8-1), indicating a timespan of at least

~100ky when the hydrothermal system remained at temperatures >350°C, the cliosure

temperature for phlogopite. Two samples of biotite infill have identical ages of 3.20 ± 0.04Ma and

3.18 ± 0.02Ma. The age dates for phlogopite and biotite indicate that the potassic alteration

assemblage K-feldspar ± biotite began at 3.28 ± 0.02Ma and continued to 3.18 ± 0.02Ma. The

rapid age transition for potassic alteration relative to the older phlogopite samples may indicate a

more rapid transition through the closure temperatures of phlogopite and biotite. A single

muscovite sample with an age of 3.18 ± 0.02Ma provides an oldest age for the zoned quartz-pyrite

alteration, which is within error of the potassic group biotite ages. However, a second, potentially

unreliable age for muscovite is older at 3.45 ± 0.06Ma and apparently contemporaneous with

early skarn alteration. An age for molybdenite post-dating covellite has been determined from Re-

Os techniques as 3.02 ± 0.02Ma (Mathur, pers comm.), which is the average of two analyses from

the same sample as presented in Mathur *et al.* (2005). The two analyses of covellite-pyrite

mineralisation from Kucing Liar have ages of 3.01 ± 0.02Ma and 3.03 ± 0.02Ma in Mathur *et al.*,

(2005) are from the sample KL42-2 440.5m and are given geological and paragenetic context

here. These ages suggest that quartz-pyrite alteration took no longer than 200ky.

Geochronology of the Ertsberg Mining District

Ages derived from magmatic biotite collected from intrusive bodies demonstrate a distinct period

of magmatic activity between ~4.5 and ~2.5Ma (Table 8-3). The oldest intrusive rock is the Kay

intrusion, situated between the Kucing Liar and Big Gossan deposits, at 4.44 ± 0.1Ma and the

youngest is a component of the Ertsberg intrusion at 2.65 ± 0.12Ma. Ertsberg ages (~3.09-

2.65Ma) overlap with the younger part of the total range of Grasberg ages (~3.33-2.77Ma). The

Karume intrusion, situated between the two, has an age 3.13 ± 0.09Ma, overlaps with ages from

_____

both the Grasberg and Ertsberg igneous suites (Table 8-3). The single date of 3.51 ± 0.02Ma from the Lembah Tembaga porphyry is contemporaneous with a date from the Wanagon sill (3.46 ± 0.06Ma). A second age from the Wanagon body is older at 3.81 ± 0.06Ma. The North Grasberg intrusion also has two inconsistent ages; the older age of 3.5 ± 0.23Ma overlaps with ages from Lembah Tembaga and Wanagon, while the younger age of 3.04 ± 0.14Ma coincides with the middle of range from the Grasberg suite (Table 8-3).

Ages for alteration minerals in the two complexes display a continuum of hydrothermal activity, though the Ertsberg Igneous Suite was mineralised significantly later than Grasberg as deduced from Re-Os dating of sulphide material, which indicates younger ages for Ertsberg than Grasberg (Figure 8-11). An oldest constraint on Grasberg copper mineralisation of 3.07 ± 0.01Ma is proposed based on $^{40}Ar/^{39}Ar$ geochronology of coarse brown phlogopite immediately preceding chalcopyrite mineralisation in the paragenesis (Pollard and Taylor, 2001). A younger age of 2.9 ± 0.3Ma is provided for Grasberg copper mineralisation based on a Re-Os isochron age (Mathur *et al.*, 2000). An $^{39}Ar/^{39}Ar$ age of 2.82 ± 0.04Ma for phlogopite from Big Gossan (Prendergast *et al.*, 2005) indicates that this deposit is similar in age to the EESS, while an $^{40}Ar/^{39}Ar$ age of 3.62 ± 0.06Ma for K-feldspar from Wanagon indicates that this deposit is older than Grasberg, implying that the pyrite-Au-As-Zn-Bi-Te is either a much later overprint related to EESS mineralisation, or that this type of mineralisation developed at two distinct periods.

Sillitoe (1994) suggests that the maximum timespan of a single hydrothermal system is 1Ma. The Kucing Liar system appears to be half that at 500ky, but was a single event within a period of regional igneous activity lasting 1.5 Ma. Two other major hydrothermal events are related to the Grasberg Igneous Complex and the Ertsberg Intrusive Suite. The Kucing Liar system may be partially related to the Grasberg system though mineralised assemblages have different ages. Porphyry emplacement appears to predate and be contemporaneous with hydrothermal alteration, while the Kucing Liar mineralisation is contemporaneous with early stages of silicate alteration but older than mineralisation assemblages at Grasberg.
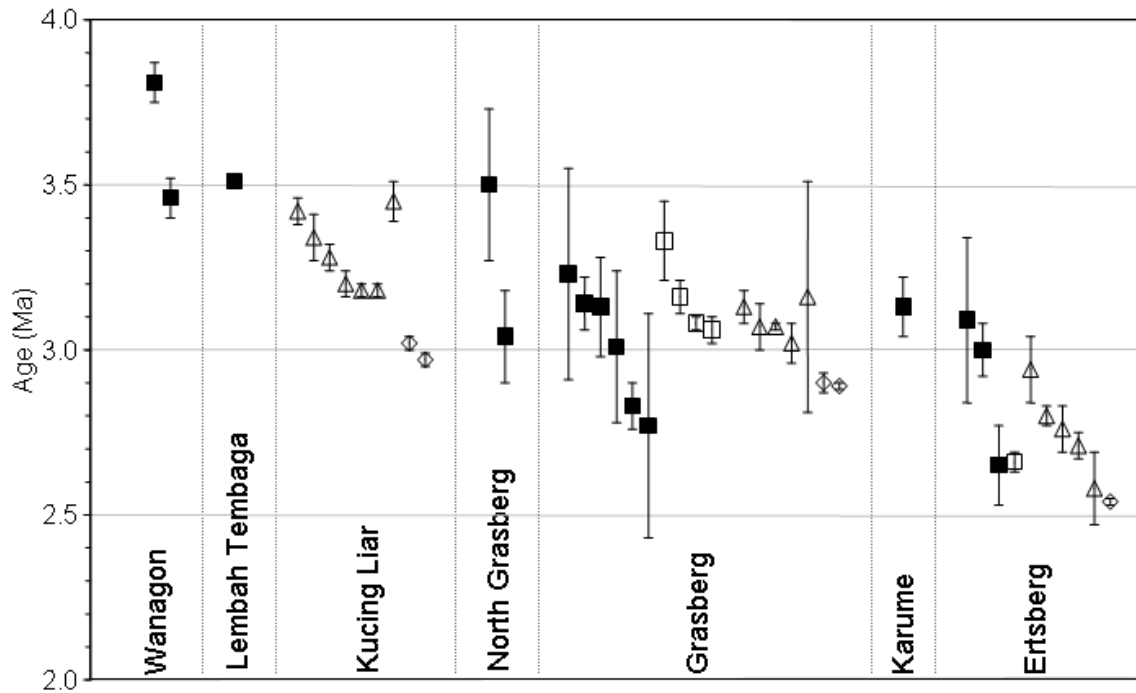
Figure 8-11 Geochronology of the Ertsberg Mining District

Ages of magmatic biotite and hydrothermal green phlogopite, brown phlogopite, muscovite and molybdenite samples collected in the district (this study (Chapter 2); McDowell et al., 1996; Pollard and Taylor, 2001 (Chapter 1)). Squares are magmatic ages, filled indicates a K-Ar ages while open indicate $^{40}Ar\text{-}^{39\text{€}}Ar$ ages. Triangles are hydrothermal minerals, all of which are $^{40}Ar\text{-}^{39}Ar$ ages. Diamonds are Re-Os ages for sulphides. Kucing Liar ages are presented in paragenetic sequence, while all other samples are organised by spatial association and age.

Table 8-2 Geochronology of Ertsberg Mining District hydrothermal minerals

Sample	System	Method	Mineral	Age (Ma)
A96-43-5 275.0m	Grasberg	$^{40}Ar\text{-}^{39}Ar$	Muscovite	3.16 ± 0.35
A96-43-5 68.5m	Grasberg (Kali)	$^{40}Ar\text{-}^{39}Ar$	Biotite	3.13 ± 0.05
A96-41-3 92.5m	Grasberg	$^{40}Ar\text{-}^{39}Ar$	Biotite	3.07 ± 0.01
A96-36-4 150.1m	Grasberg	$^{40}Ar\text{-}^{39}Ar$	Biotite	3.02 ± 0.06
Unnamed	Grasberg	Re-Os	Molybdenite	2.90 ± 0.30
Unnamed	Grasberg	Re-Os	Sulphides	2.89 ± 0.10
B42 DOZ	Ertsberg East	$^{40}Ar\text{-}^{39}Ar$	Phlogopite	2.94 ± 0.10
B43 GBT-A	Ertsberg East	$^{40}Ar\text{-}^{39}Ar$	Phlogopite	2.80 ± 0.03
B41 DOZ	Ertsberg East	$^{40}Ar\text{-}^{39}Ar$	Phlogopite	2.76 ± 0.07
DZ5-04 290.2m	Ertsberg East	$^{40}Ar\text{-}^{39}Ar$	Biotite	2.71 ± 0.04
Unnamed	Ertsberg East	Re-Os	Molybdenite	2.54 ± 0.10

Sources of data: Pollard et al. (2001) and Mathur et al. (2005)

Table 8-3 Geochronology of Ertsberg Mining District intrusions

Sample	System	Method	Mineral	Age (Ma)
1001	Ertsberg East	K-Ar	Biotite	3.00 ± 0.08
1002	Ertsberg East	K-Ar	Biotite	2.65 ± 0.12
1003	Ertsberg East	K-Ar	Biotite	3.09 ± 0.25
DZ5-06 269.3m	Ertsberg East	^{40}Ar-^{39}Ar	Biotite	2.66 ± 0.03
2001	Grasberg	K-Ar	Biotite	2.83 ± 0.07
2002	Grasberg	K-Ar	Biotite	2.77 ± 0.34
2003	Grasberg	K-Ar	Biotite	3.01 ± 0.23
2004	Grasberg	K-Ar	Biotite	3.14 ± 0.08
2005	Grasberg	K-Ar	Biotite	3.13 ± 0.15
2006	Grasberg	K-Ar	Biotite	3.23 ± 0.32
A96-40-5 95.0m	Grasberg	^{40}Ar-^{39}Ar	Biotite	3.33 ± 0.12
A96-41-2 172.5	Grasberg	^{40}Ar-^{39}Ar	Biotite	3.06 ± 0.04
A96-43-5 57.3m	Grasberg (Kali)	^{40}Ar-^{39}Ar	Biotite	3.16 ± 0.05
3001	North Grasberg	K-Ar	Biotite	3.50 ± 0.23
3002	North Grasberg	K-Ar	Biotite	3.04 ± 0.14
LT 1-5 953m	Lembah Tembaga	^{40}Ar-^{39}Ar	Biotite	3.51 ± 0.02
4001	Wanagon	K-Ar	Biotite	3.81 ± 0.06
4002	Wanagon	K-Ar	Biotite	3.46 ± 0.06
5001	Karume	K-Ar	Biotite	3.13 ± 0.09
6001	Kay	K-Ar	Biotite	4.44 ± 0.10

Sources of data: McDowell et al (1996) for K-Ar data, Pollard and Taylor (2001) for ^{40}Ar-^{39}Ar data. The Kali dyke sample from Grasberg is considered a younger age for the complex as they are the last intrusive phase.

9 Discussion

This discussion chapter aims to integrate the various results of the research program. Of interest in the first section is the nature of deformation and its relationship to tectonic forces, as well as the influence the deformation mechanism has on the emplacement of magmatic-hydrothermal systems. The second section intends to develop a model for the hydrothermal evolution, which is consistent with the results of fluid inclusion, stable isotope and metal distribution studies. These data indicate that zoned alteration mineralogy and base and precious metal mineralisation are related to phase separation and fluid mixing. The final section aims to compare and contrast the Kucing Liar genetic model with existing models of porphyry-epithermal mineralisation.

_____

9.1 TECTONIC-MAGMATIC SETTING OF FLUID INFILTRATION

The major results that relate to tectonic models are the local structural setting and the geochronology of intrusive suites and spatially related hydrothermal systems. As limited data has been collected in relation to fault vectors, published literature concerning deformation mechanisms are used to review the results.

9.1.1   Tectonic transition and porphyry emplacement

The interpreted local tectonic history involves a change from folding and thrusting to more lateral fault displacement (Quarles van Ufford, 1996; Sapiie and Cloos, 2004). A change in deformation style can be brought about by a change in convergence direction of tectonic plates as shown by experiments for various collision angles at various obliquities (Casas *et al.*, 2001). A sharp contrast in deformation styles occurs at convergence angles between 15º and 30º (Figure 9-1). At angles ≤15º strike-slip displacement occurred on 'R' and 'Y'-type shears and no significant uplift was observed, while for convergence angles ≥30º an uplift zone bound by two fault zones formed. The strike-slip component of displacement decreased with increasing convergence angle, as did the number of 'R'-type faults. Arc-oblique 'P'-type orientations tend to dominate in the back limb of the uplifted zone and have been reproduced in experimental modelling of thrust environments. The change from reverse to strike-slip faults is caused by a change in convergence angle below 30º (Figure 9-1). Such change in convergence angle has been postulated for the development of New Guinea where southerly directions apparently changed to west southwesterly at ~5Ma (Sapiie and Cloos, 2004), immediately preceding igneous activity in the Ertsberg Mining District which persisted from 4-2Ma (Chapter 8).

Change in deformation styles from folding and reverse faulting to lateral fault movement may have driven fluid migration and could account for the temporal clustering of magmatic hydrothermal systems. The Idenberg Fault Zone was evidently active during fluid infiltration as revealed by the different offsets for stratigraphy and skarn (Chapter 4) as well as permeability

considerations which require continued generation of secondary porosity through fracturing to offset infilling of fractures with mineral growth (Cox et al., 2001). The expected stress differential and associated relaxation of confining pressures due to deformation changes arising from tectonic transitions could facilitate magma ascent (Tosdal and Richards, 2001), as well as causing fluid redistribution (Sibson, 2001). An association of porphyry emplacement with tectonic transition is consistent with general models for gold-producing porphyry episodes which are considered to be short-lived and commonly formed as an end-stage of arc development (Sillitoe, 1997).
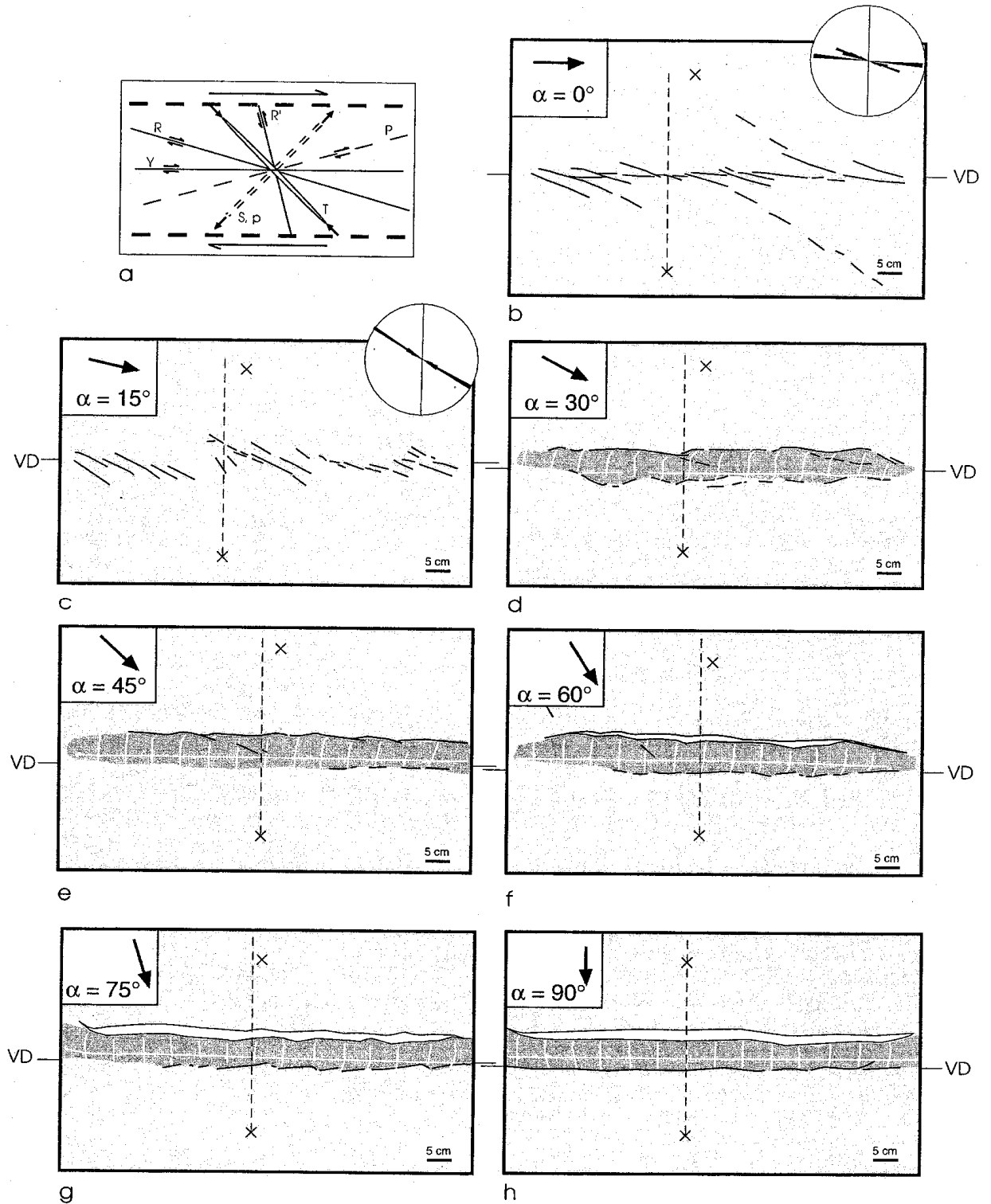
Figure 9-1 Analogue model of deformation front for various convergence angles

The figures range from pure strike-slip (a) to pure thrusting (h). The shadowed zones represent regions of uplift. The predominance of Reidel (R) structures for low convergence angles (α) is supported by models of strike-slip displacement (reproduced from Casas et al., 2001).

_____

9.1.2   Progressive deformation and structural geometry

Kucing Liar is centred on the intersection between a complex fault zone and a heterogeneous litho-stratigraphic section containing sandstone, calcareous shale and thinly-bedded limestone. The main Kucing Liar mineralized zone lies in the Ekmai Limestone and the lower part of the Waripi Limestone where the sequence is displaced by the Idenberg Fault Zone. Minor alteration and mineralization (mainly covellite-bearing), is hosted by the upper sandstone member of the Waripi Limestone (Chapter 4). This stratigraphical control of ore deposition is repeated in other mineralized systems in the Ertsberg Mining District (Chapter 1). However, the localisation of hydrothermal systems requires both a primary fluid focus such as the Idenberg Fault Zone, as well as a favourable local environment of high permeability, such as the thinly-bedded limestone in the lower Waripi Limestone. Neither faults nor the units which act as a local host are uniformly mineralized, a combination of fault and stratigraphic control being required. Alteration and mineralization at the Nena deposit in Papua New Guinea are concentrated at the intersection of a vertical fault with a permeable coarse pyroclastic horizon (Bainbridge *et al.*, 1998). The Lepanto ore body in the Philippines occurs at the intersection of the Lepanto Fault and an unconformable contact between dacite and volcaniclastic rocks (Hedenquist *et al.*, 1998).

Fluid flow was focused along major stratigraphic contacts in stratabound breccias, probably produced by deformation of heterogeneous stratigraphy as well as where the favourable orientation of stratigraphic layering relative to fault movement resulted in tensional strain (Chapter 4). Fluid infiltration most likely occurred during active fault movement as indicated by continued development of new veins and fracture infill. The Idenberg Fault Zone is characterised by a number of internal offsets (Chapter 4) that have different asymmetry and resulted in >600m of vertical displacement based on the relative positions of distinctive marker horizons (Chapter 2). While there is enough evidence to indicate both reverse-slip and strike-slip movement in the Idenberg Fault Zone, it is unclear if it represents separate deformation episodes or was combined in an oblique-slip system. The development of offsets within the primary fault zone is the result of

_____

progressive deformation and has resulted in the concentration of late stage hydrothermal activity (Chapter 4) including copper-gold mineralization (Chapter 5) within complex fault jogs. The Idenberg Fault Zone possesses two distinct offsets as defined by lithological distribution models (Chapter 4). The displacement of stratigraphy is evident by identification of marker horizons and record a relative vertical offset of ~600m. Skarn alteration is also displaced across the Idenberg Fault Zone although the stratigraphy on either side is altered at different stratigraphic levels (300m difference). Based on the assumption that alteration would occur at similar levels on either side of the fault zone in similar rock types, the difference between lithological and skarn displacement indicates skarn formed after substantial fault movement had already occurred.

Offsets or jogs in fault zones are either dilatant or compressional structures (Sibson, 1989) depending on their orientation and the direction of movement. The visible displacement of key marker horizons within the Kucing Liar stratigraphy suggests the Idenberg Fault Zone is a steep reverse fault. However, lateral movement for the Idenberg Fault Zone could also account for the apparent vertical displacement of stratigraphy. For instance, left-lateral movement of stratigraphy folded about a west-northwest plunging fold axis, such as occurs in the Yellow Valley Syncline, would result in apparent north side up vertical displacement. Fault offsets or jogs may form from the intersection of and incorporation of older structures with younger structures (e.g. Hildenbrand et al., 2000), or from progressive deformation (Dube and Guha, 1992). The offset within the Idenberg Fault Zone may represent two periods of faulting in which an early wide vertical fault has been intersected and offset by northeast dipping structures. If this were the case, another wide subvertical fault segment should be present at deeper levels on the southwestern side of the fault zone. Due to complex lithological relationships combined with low data density, the existence of a fault at this location is not ruled out. A second option for explaining the Idenberg Fault Zone geometry is that the pattern of narrow and wide structures is the result of progressive deformation. A left-lateral strike-slip history involving an early dilational jog followed by a later compressional jog would be consistent with published deformation models. Experimental studies of continuously deforming fault zones (Tchalenko, 1970; Dube and Guha, 1992) indicate an evolution of fault

structure from:

1. low angle tensional ('R'-type) structures forming at peak shear resistance in dilational orientations accompanied by a conjugate high angle fractures ('R1'-type) that are also dilational

2. oblique restraining, or compressional ('P'-type) shears form following peak shear strength in an asymmetric orientation to the R-type fractures, and finally,

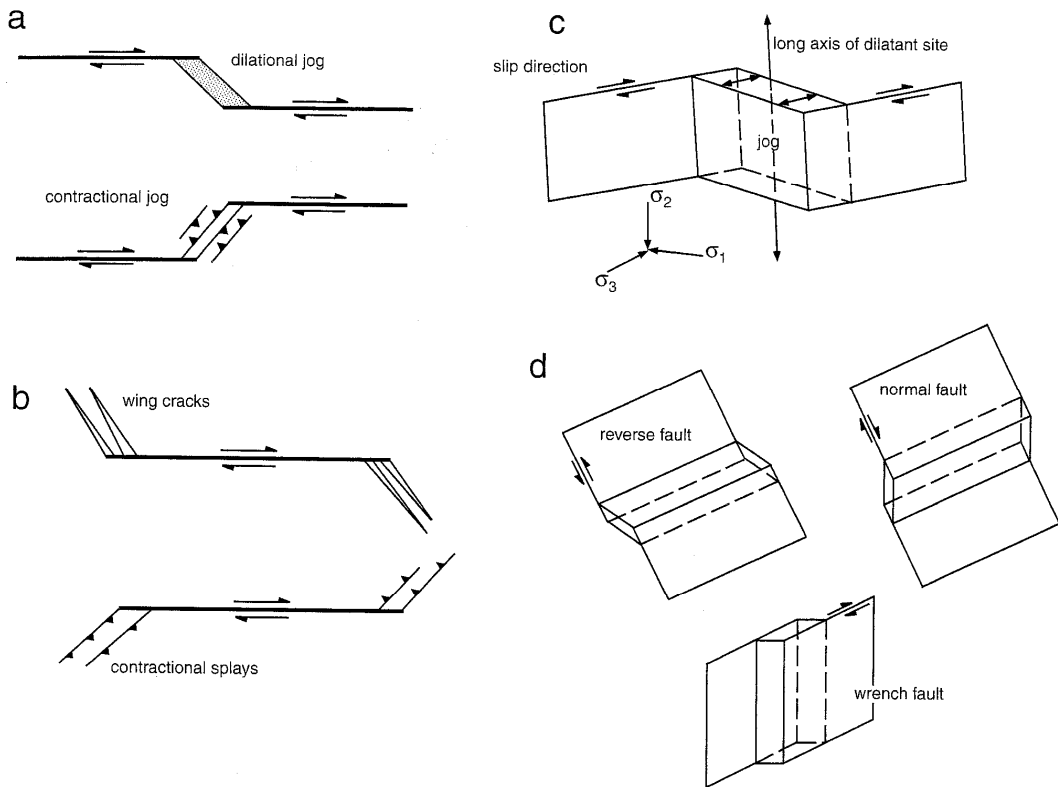3. throughgoing ('D'- or 'Y'-type) fault structures (Figure 9-4).

Figure 9-2 Geometry and structural detail of fault jogs

(a) Geometry of contractional and dilatant jogs. (b) Wing cracks and contractional splays developed around fault terminations (c) Geometry of a dilatant jog relative to fault slip direction (d) Orientation of jogs in contractional, extensional and lateral movement vectors. Figure reproduced from Cox et al., (2001). Note that the Idenberg Fault Zone is very similar in geometry to the normal fault geometry, however, this relationship is ruled out due to inconsistency with the only possible movement vectors which are reverse and left-lateral.
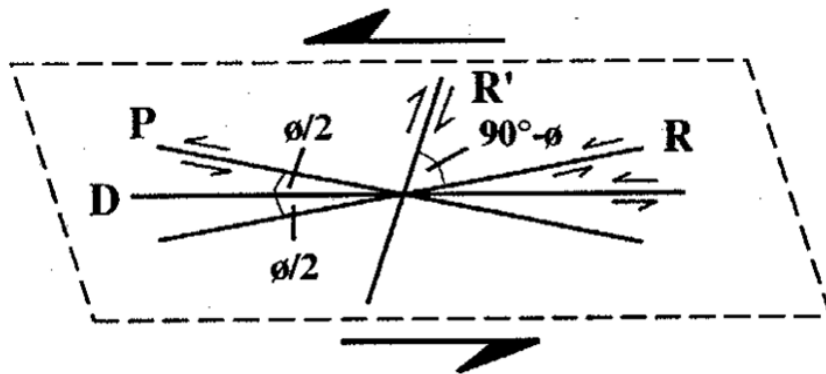
Figure 9-3 Naming convention for structures present in a left lateral fault-slip system
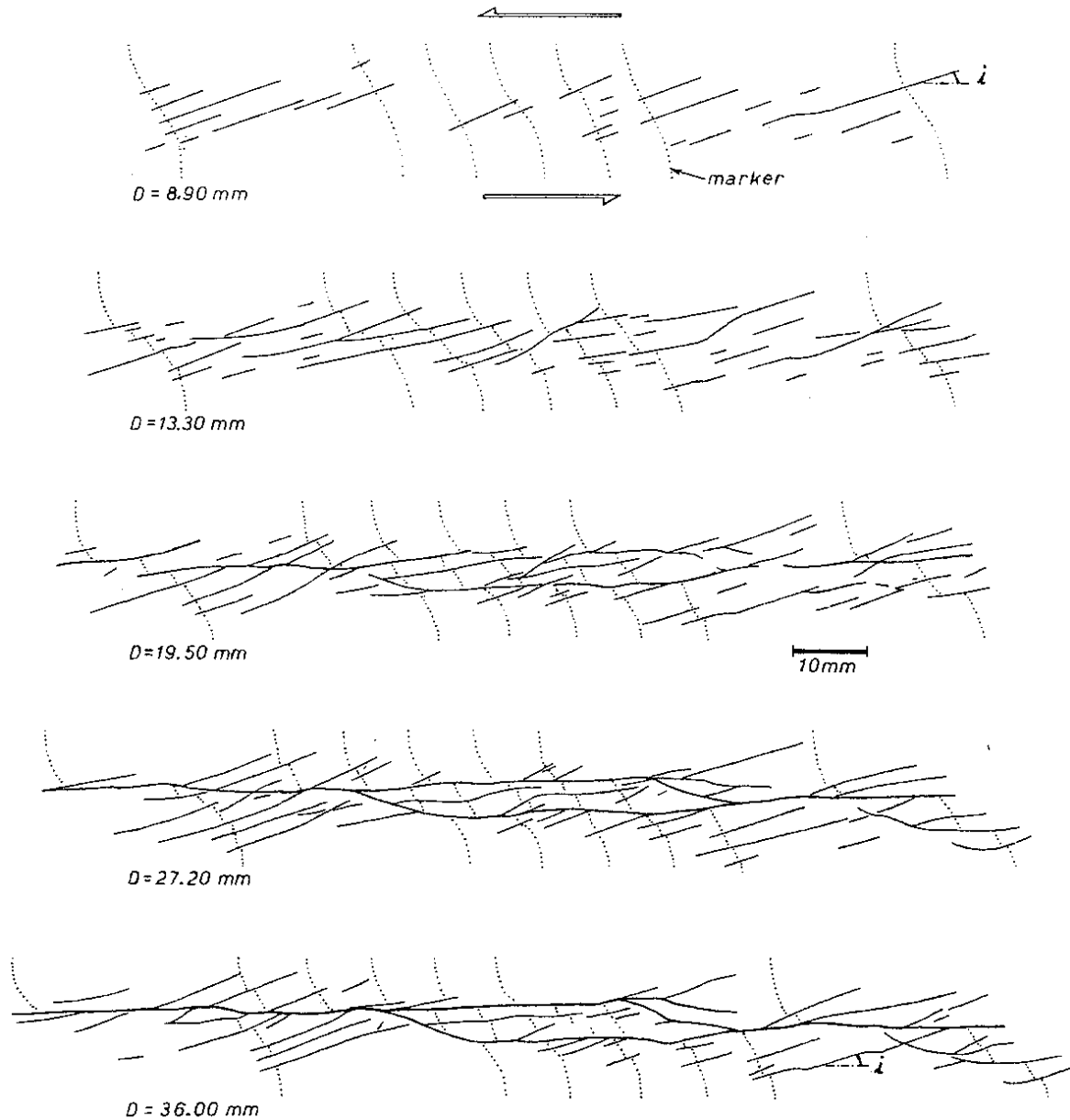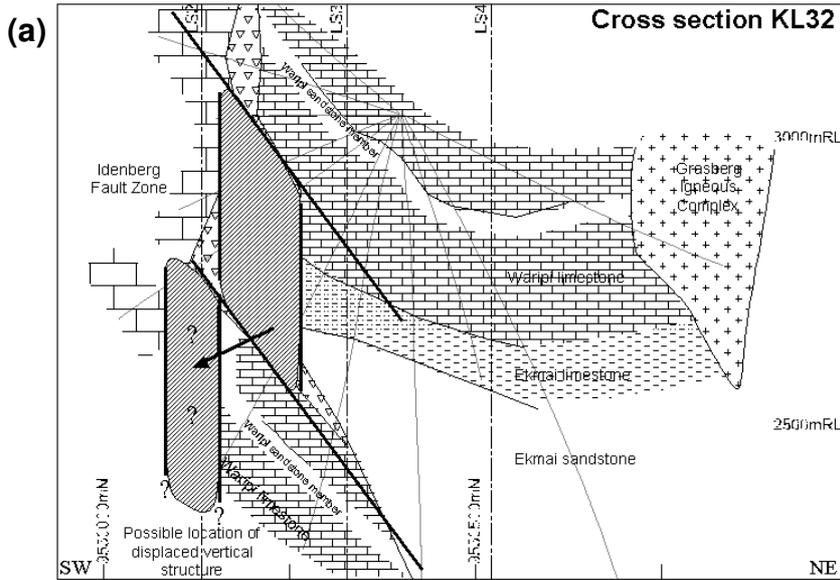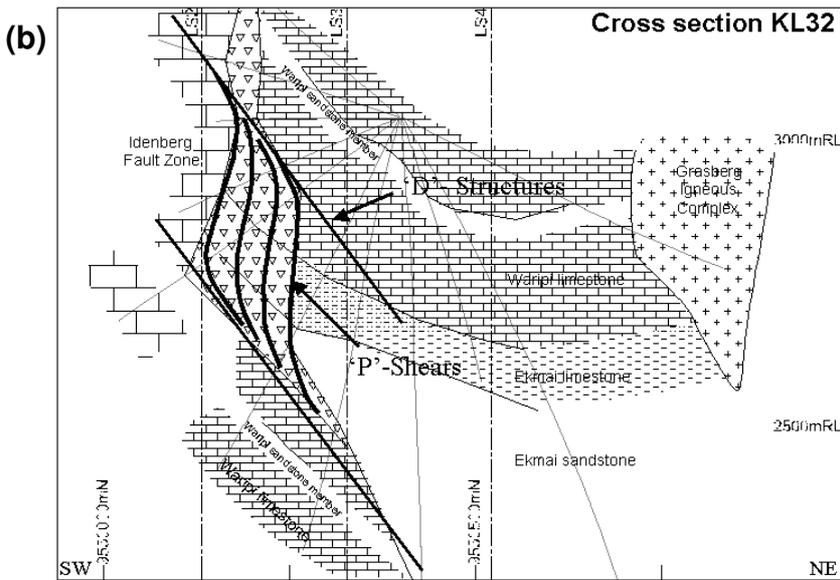
Adapted from Tchalenko (1970)

Figure 9-4 Geometric characteristics of strike-slip faults

Progression of deformation features produced in experiments of left-lateral fault displacement. D=distance of displacement. Reproduced from Tchalenko (1970).
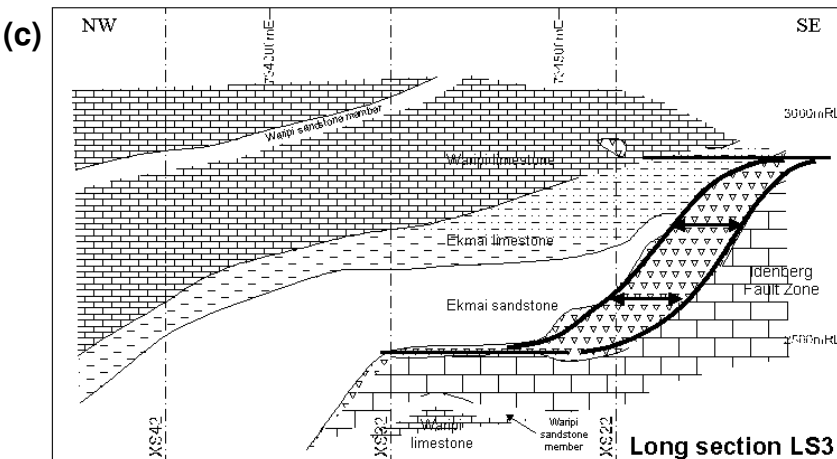
Figure 9-5 Speculative models for development of structral offset in Idenberg Fault Zone

Three alternatives for the development of offsets in the Idenberg Fault Zone. (a) A model of two-phase faulting where an early near-vertical fault is overprinted and offset by steeply dipping faults. The lack of data in the expected location of the displaced fault zone means that this model is not precluded. (b) A compressional or contractional offset where progressive deformation of a steeply-dipping fault zone results in a stepover between parallel fault structures. The model implies that each line through the offset is a small thrust-fault. These types of structures will eventually seize up and progress to throughgoing structures (c) The small offset visible in long section must be a dilational offset whether produced during vertical or left lateral movement. The lack of later paragenetic minerals in this offset suggests it formed during vertical displacement. This is supported by the association of early garnet with this structure.

9.2 FLUID EVOLUTION LEADING TO HYDROTHERMAL MINERALIZATION

The Kucing Liar deposit is associated with a complex alteration succession which includes some 26 major minerals in distinct assemblages (Chapter 2). The hydrothermal minerals can be divided into four distinct groups which include:

- prograde and retrograde calcic and magnesian skarn

- potassic-magnetite alteration plus retrograde skarn

- silicification ± muscovite and anhydrite alteration

- sulphide mineralization, including chalcopyrite or covellite ± pyrite zones plus galena-sphalerite

The relationship of prograde skarn in limestone and hornfels development in shale is unclear. Both exhibit a similar early paragenetic history where clinopyroxene ± garnet is overprinted by K-feldspar ± biotite (Chapter 2). Timing relationships between the two copper-bearing sulphides and pyrite indicate that they must be near-contemporaneous (Chapter 2), which supports the observed metal zoning. Overprinting of an early chalcopyrite-bearing mineralized zone by later covellite-bearing mineralization should produce a new metal zonation, or at least some interference patterns, but none is observed (Chapter 5).

### 9.2.1 The collapse of magmatic-hydrothermal systems

The hydrothermal mineral paragenesis records a decrease in temperature conditions, from >600°C to <400°C, which may have been influenced by fluid mixing in the Idenberg Fault Zone. Fluid conditions for quartz alteration that overprints skarn and potassic alteration are well constrained by fluid inclusions in quartz which suggest temperatures of formation <420°C. Quartz alteration also hosts lower temperature (~300°C) fluid inclusions though these are probably not related to primary growth and could be interpreted to represent later overprinting fluids. Temperatures >400°C at shallow depths mark the normal limit for the brittle behaviour of rock types (e.g. Meinert *et al.*, 2003). Ductile behaviour seals the system from significant interaction with local

_____

waters (Fournier, 1996; Meinert *et al.*, 2003), while brittle conditions would be expected to promote infiltration by external fluids. This is in agreement with stable isotope data which record shifts toward lower $\delta^{18}O_{FLUID}$ values during retrograde skarn and quartz alteration (Chapter 8).

The water associated with skarn and potassic alteration was clearly magmatic (Chapter 8), while later quartz and anhydrite alteration were caused by distinctly lower $\delta^{18}O$ fluids which are believed to have been close to local meteoric water (Chapter 8). Quartz alteration is closely associated with the Idenberg Fault Zone, and this association may indicate that structural evolution was a driving force behind fluid mixing and dilution. Fluid dilution in the Idenberg Fault Zone may also have been promoted by phase separation of magmatic fluids. Phase separation may occur during sudden pressure drops such as massive hydrofracturing, sudden removal of lithostatic load (sector collapse of a volcanic edifice), or rupturing at the brittle-ductile transition (Fournier, 1999). If phase separation of hydrothermal fluids did occur at Kucing Liar, it was probably a consequence of the low hydrostatic pressures in the Idenberg Fault Zone during active deformation. Hypersaline fluids, such as those generated by phase separation and that produced quartz alteration, may not pass across the ductile-brittle boundary, due to their high density and viscosity (Hedenquist *et al.*, 1998). However, the ductile-brittle boundary is permeable to buoyant, low-salinity and low-viscosity vapour, as evidenced from passive degassing in volcanoes unassociated with eruptive events (Hedenquist *et al.*, 1998).

9.2.2   Effect of fluid mixing on ore chemistry

The combination of lower temperatures and increased external fluid input is expected to have had a significant impact on the hydrothermal chemistry, resulting in conditions favourable for sulphide deposition and high sulphidation mineralization. A higher degree of local water interaction is believed to have promoted quartz precipitation below 420°C from highly mixed waters the Idenberg Fault Zone. The effect of reduced temperatures in the system was probably to promote hydrolysis-disproportionation of SO_2 in the magmatic fluids, a process which occurs at ~400°C (e.g. Seedorff et al., 2005). This process is a hydrolysis reaction defined as:

$$4SO_2 + 4H_2O \rightarrow H_2S + 3H_2SO_4$$
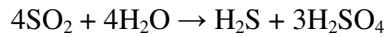
Anhydrite is derived from the reaction of sulphuric acid with calcium-bearing fluids which generate anhydrite via the reaction:

$$CaCl_2 + H_2SO_4 \rightarrow CaSO_4 + 2HCl$$
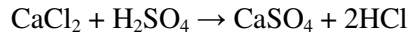
(Burnham, 1979). The effect of producing anhydrite is to generate hydrochloric acid which is involved in the formation of the assemblage quartz ± muscovite from K-feldspar by the reaction:

$$3KAlSi_3O_8 + 2HCl \leftrightarrow KAl_3Si_3O_{10}(OH)_2 + 6SiO_2 + 2KCl.$$

The development of chalcopyrite and the accompanied sulphidation of magnetite are achieved via reactions:

$$CuCl_2 + FeCl_2 + 2H_2S \rightarrow CuFeS_2 + 4HCl$$

$$Fe_3O_4 + 6H_2S + O_2 \rightarrow 3FeS_2 + 6H_2O$$
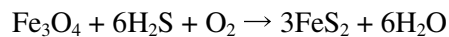
Precipitation of base metals from brine is based on a H_2S interaction via similar reactions to that above. Advanced dilution would have exacerbated the H_2S development through continued cooling and availability of H_2O, resulting in the quartz-muscovite-anhydrite assemblage as well as driving metal precipitation from brines and sulphidation of magnetite to form extensive pyrite and chalcopyrite development. The development of the assemblage quartz ± muscovite, anhydrite has been linked to the process of sulphur disproportionation (Burnham, 1979, Tosdal and Richards, 2001).

Low salinity magmatic fluids related to covellite mineralization were circulating at temperatures around 300°C (Chapter 6). Phase separation was probably limited to the quartz alteration process (Chapter 6), which in turn was closely associated with movement of the Idenberg Fault Zone

_____

(Chapter 4) and related fluid mixing (Chapter 8). Therefore the origin of Au-As-(Sb-Hg) low

sulphidation mineralization, which is concentrated at the upper zones of Kucing Liar, is believed

to be related to the interaction between low density phases and local meteoric waters due to

Idenberg Fault Zone movement. Extraction of a low-density magmatic phase may have

preferentially partitioned Au, Sb and As as bisulphide complexes (Bessinger and Apps, 2003;

Heinrich *et al.*, 2004). Interaction of this low density phase with local meteoric waters would have

caused the "vapour" to contract to form a low salinity liquid, as preserved in fluid inclusions in

fluorite related to covellite (Chapter 7). Heinrich *et al.*, (2004) have suggested that contracted

magmatic vapour may be in equilibrium with muscovite. A model whereby low density vapours

are contracted back to a liquid form following cooling due to contact with local meteoric water

(*cf*. Mancano and Campbell, 1995) is consistent with the observed pattern of low salinity liquids

related to covellite-bearing mineralization hosted in quartz alteration that previously developed

from high density brines. The expected high-acidity fluid derived from mixing of magmatic

vapour and meteoric water would form kaolinite, however, the carbonate wall rocks would have

had a high capacity for acid buffering. The effectiveness of fluid mixing in the mineralization

process is demonstrated by the almost total precipitation of saturated gold from magmatic brine

that is diluted 10-fold with meteoric fluid containing negligible chloride (Gammons and

Williams-Jones, 1997). Calculations also indicate that 99% of copper partitioned into the aqueous

fluid precipitates as the fluid is cooled to 250ºC, most between 350-250ºC window, though copper

does precipitate at higher temperatures from NaCl-saturated fluids derived from shallow, low

pressure systems (Cline and Bodnar, 1991).

9.3 KUCING LIAR IN THE CONTINUUM OF PORPHYRY-RELATED ORE SYSTEMS

9.3.1   Classification of porphyry-epithermal ores

Porphyry-related ore deposits are a very common deposit throughout the Pacific Rim with numerous examples in New Guinea, the Philippines, the Rocky Mountains of Canada and USA, Central America, Peru and Chile. There are a number of classes that have distinct mineralization styles and gangue alteration assemblages that are all ascribed an origin related to porphyry magmas (Figure 9-6).

1. Porphyry-hosted mineralized systems are common with chalcopyrite ± bornite hosted in quartz stockworks in potassic alteration zones

2. Skarn deposits are frequently found at the margins of the intrusive bodies and are divided into proximal and distal varieties

3. High sulphidation epithermal deposits are typically external to porphyry stocks and have typical assemblages of covellite, enargite, digenite, chalcocite related to advanced argillic alteration characterised by alunite, kaolinite and diaspore.

4. Base metal veins (Au-As-Sb ± Ag-Zn-Pb) are common at more distal locations from the porphyry stocks where mineralization is related to locally massive sulphide deposition

5. Low sulphidation epithermal Au-Ag deposits are distal to hypothesized coeval porphyry stocks

Kucing Liar contains zones with characteristics similar to the first four of these styles that represent a chemically zoned system. The chalcopyrite (-magnetite) ores is typical of proximal Cu-Au skarns, whereas the quartz-muscovite-covellite is typical of high sulphidation epithermal in phyllic environments (Hedenquist *et al.*, 1997) and the locally massive pyrite bodies with

accompanying enargite and auriferous arsenian pyrite, possibly with tennantite are similar to descriptions of base metal veins such as is the major ore source at Butte, Montana (*cf.* Einaudi et al., 2003). One abnormality is that high sulphidation mineralization at Kucing Liar is related to silica-pyrite-muscovite (phyllic) style alteration rather than advanced argillic alteration. This may because the pH was not low enough to form kaolinite and alunite, most likely due to buffering by carbonate rocks. Alternatively, covellite ± pyrite ± enargite may have formed in equilibrium with muscovite. Heinrich et al., (2004) have now suggested a process involving contraction of magmatic vapour which is predicted to be in equilibrium with muscovite. Muscovite-stable alteration at Lepanto-Far Southeast was associated with water cooler, and less saline than that responsible for only slightly older potassic alteration.

As the primary minerals of economic interest tend to be sulphides, discrimination of conditions tends to be based on the concept of sulphidation, or the oxidation state of the sulphur species. This condition will be based on both the fS_2, fO_2 and temperature conditions (Figure 9-7). The porphyry skarn ore represented by chalcopyrite ± bornite developed under low to intermediate sulphidation conditions, in contrast to those of the high sulphidation assemblage covellite ± enargite (*cf.* Sillitoe and Hedenquist, 2003). Chalcopyrite precipitation at Bajo de la Alumbrera (Argentina) is constrained to a temperature window between 400-320°C (Ulrich *et al.*, 2001b) derived from Cu concentrations measured in fluid inclusions, and mineralization at Far Southeast is reported at ~500°C deposited from brines (Mancano and Campbell, 1995). The conditions of intermediate sulphidation are within chalcopyrite, tetrahedrite-tennantite and Fe-poor sphalerite stability, and sulphide assemblages lack appreciable arsenopyrite and pyrrhotite. Based on the environment and conditions, it appears that Kucing Liar is a combination of porphyry skarn chalcopyrite ores, high sulphidation covellite ± enargite ores, and intermediate sulphidation base metal veins represented by auriferous arsenian pyrite and galena-sphalerite ores.
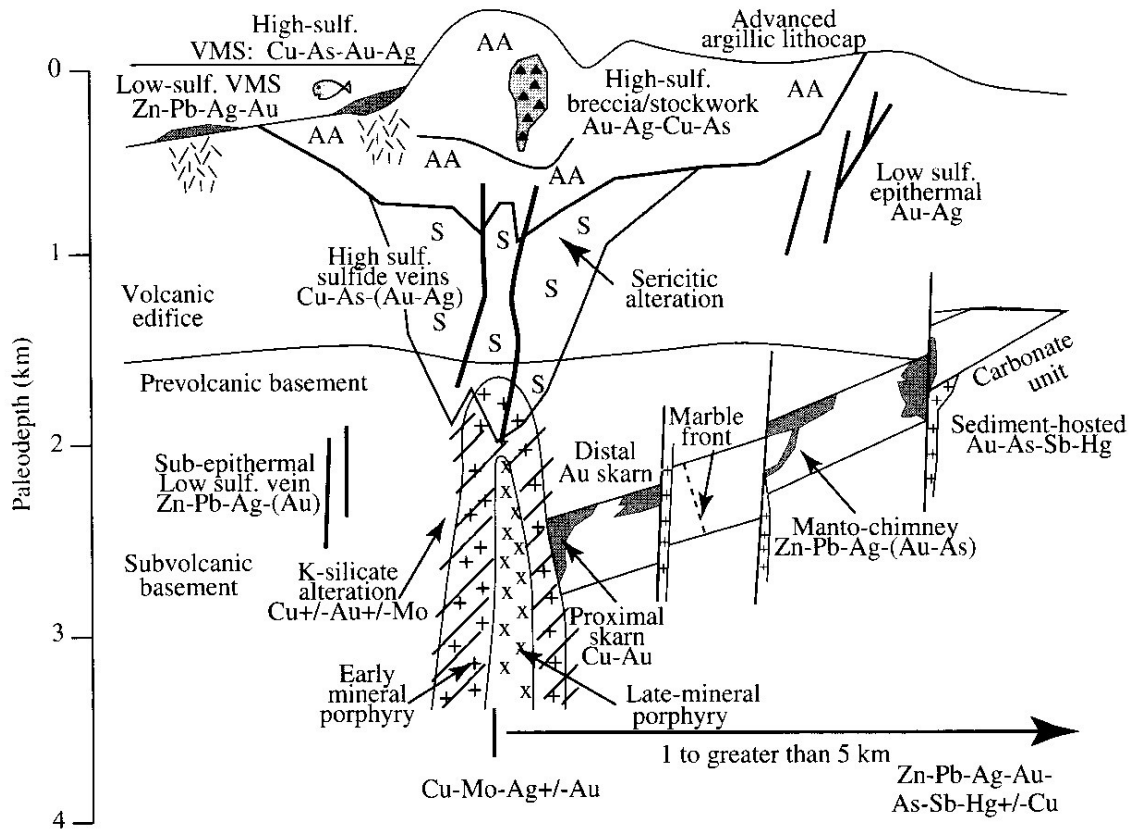
Figure 9-6 Generalised model of porphyry-related ore systems

In this model porphyry and skarn are transitional while porphyry and epithermal styles of mineralization will be distinct. It is tempting to assume from its location that Kucing Liar represents a proximal skarn at the margin of the Grasberg Igneous Complex as indicated in Figure 9-6. However, covellite-bearing mineralization at Kucing Liar preceded chalcopyrite ± pyrite ± bornite mineralization in the GIC, as constrained by biotite age of 2.94 ± 0.02 (Pollard et al., 2006). Although Kucing Liar predates the main phase of Grasberg mineralization (Chapter 8), it may actually be coeval with earlier phases of the Grasberg Igneous Complex (Macdonald and Arnold, 1989). Figure reproduced from Tosdal and Richards (2002).
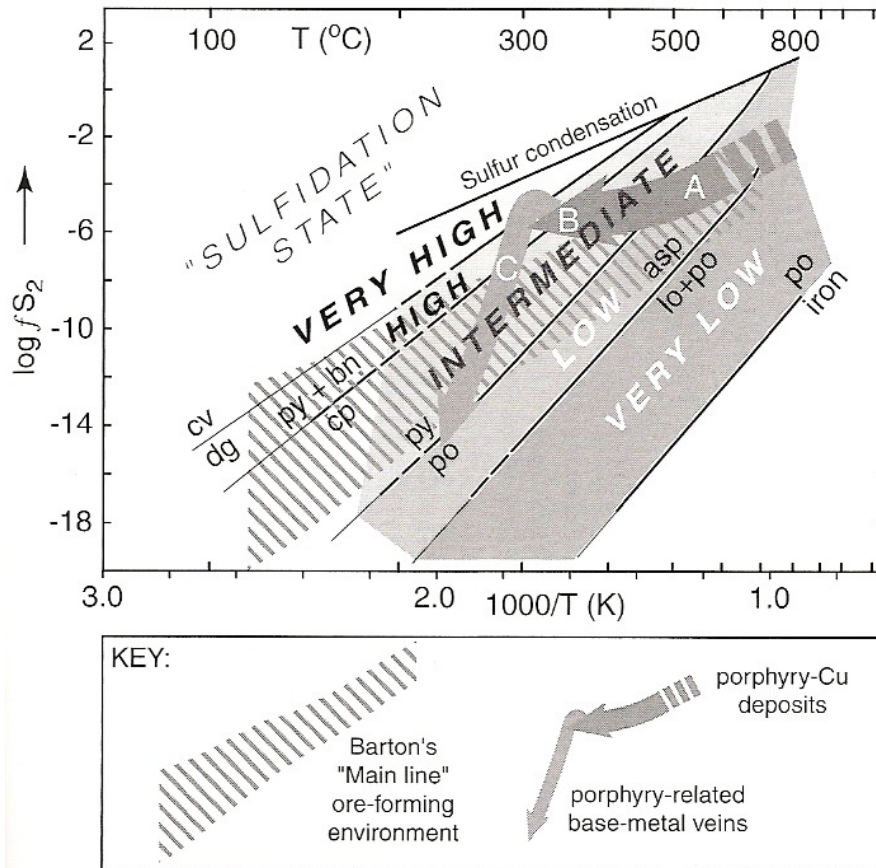
Figure 9-7 Plot of log fs_2 – Temperature for fluids in porphyry systems

This diagram is intended to illustrate the relationships between the various sulphidation states referred to within porphyry-related systems. It is apparent that sulphidation state is not directly analogous to the sulphur fugacity (fs₂). The increase in sulphidation state with decreasing temperature at constant log fs₂ may be directly related to disporpotionation of SO₂, which occurs at temperatures <400°C. The plot is considered relevant to Kucing Liar evolution as path A-B represents the progressive development of pyrrhotite-pyrite-chalcopyrite followed by pyrite ± bornite and finally digenite-covellite ± pyrite. The path B-C would represent a decrease in sulphidation state due to dilution in external water. Some fluids within Kucing Liar continued along a constant log fs₂ from point B as evidenced by the precipitation of native sulphur in some zones of covellite mineralization. Figure reproduced from Einaudi et al. (2003).

9.3.2   Juxtaposition of porphyry-epithermal systems

Porphyry-(skarn) and epithermal mineralization may be juxtaposed by overprinting of a later system due to withdrawal of the magma chamber, or by telescoping of the same process through uplift and denudation (Figure 9-8). Padilla-Garza et al. (2001) propose such a model for the Escondida copper deposit where advanced argillic alteration and high sulphidation mineralization postdate the main stage potassic-style alteration by 3Ma. The Agua Rica deposit in Argentina

_____

resembles Kucing Liar in the sense that early porphyry-style alteration and mineralization is juxtaposed with high sulphidation mineralization (Landtwing et al., 2002). However, in this case Landtwing et al. (2002) proposed that the superposition of the different styles of mineralization resulted from a protracted magmatic-hydrothermal history. This is also the case at the Collahausi district in northern Chile (Masterman et al., 2005) where it is proposed that at least 1km of denudation occurred over 1.8Myr between formation of early porphyry-style alteration at the Rosario deposit and mineralization and high sulphidation mineralisation and related advanced argillic and phyllic alteration zones. The porphyry-epithermal transition may be the result of rapid uplift and denudation (Sillitoe, 1999), a condition that is likely during convergence tectonics giving rise to volcanic activity. In this process, epithermal mineralization is not the result of a later hydrothermal system but is generated due to rapidly changing conditions during a single hydrothermal event. Such a dramatic change in conditions may be the result of volcanic processes and involve catastrophic unloading due to collapse of the volcano (e.g. van Wyk de Vries *et al.*, 2000), as is believed to have produced the large Ladolam Au resource within the Luise caldera in the Lihir Island Group. However, at Lihir, the porphyry system is dated at ~1Ma, while the mineralized epithermal system is dated to 250ky and the current geothermal system is no older than 100ky. The differences in these ages are similar to those between the different mineralized systems in the Ertsberg Mining District, indicating that they may have been sourced from different magma generations.

Based on the uplift of 1mm/yr discussed in Chapter 8, 0.5km of uplift may have taken place during the life of the Kucing Liar hydrothermal system. The transition from potassic alteration to phyllic + quartz alteration occurred within a 40ky period (Chapter 9), precluding any telescoping due to denudation in that time. Sector collapse is not ruled out though there is no hard evidence for this process. The process most likely to have caused the observed development of chalcopyrite and covellite-dominant mineralized zones at Kucing Liar is believed to be chemical changes in hydrothermal fluids (Figure 9-7). The relative sulphidation state of mineralising fluids will be controlled by interaction with external water that caused reduction of magmatic SO_2 (see Section

9.1). Figure 9-7 indicates that the mineralization in Kucing Liar may represent the transition to high sulphidation (chalcopyrite → covellite) and back to low sulphidation (such as the auriferous arsenian pyrite) due to addition of external water, which drives $f\mathrm{S}_2$ lower. The lack of variability of alteration and mineralization styles in some deposits may indicate a lack of fluid mixing, or too much mixing. The sulphur budget of a hydrothermal solution cannot be changed without external influence. Disproportionation of SO_2 would not in itself change the sulphur content, but would drive the system towards high sulphidation states at lower temperatures (Figure 9-7). A steady addition of water would lower relative sulphur content thereby maintaining a constant sulphidation state. Thus, in the case of Kucing Liar, sealing off the Idenberg Fault Zone would control the $f\mathrm{S}_2$ while fluids that escaped into the overlying rock mass would come into contact with meteoric water and have their sulphur content diluted.
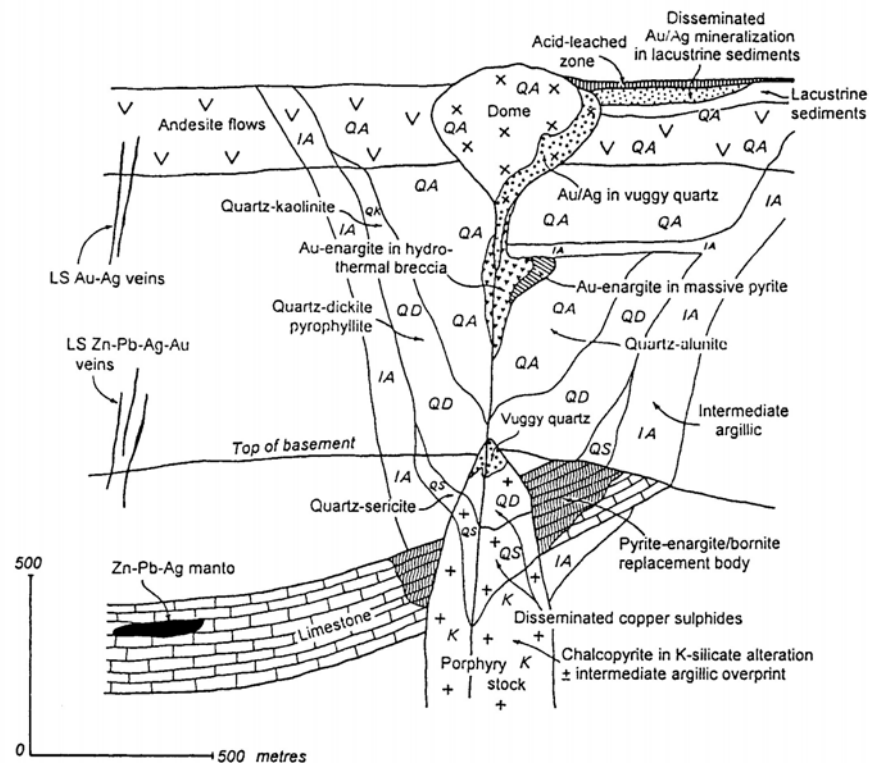
Figure 9-8 Telescoping of epithermal systems into porphyry environment

This figure illustrates how high sulphidation pyrite-enargite with associated quartz-muscovite alteration can be juxtaposed against a porphyry intrusion and its proximal skarn zone. This model requires some time lapse between skarn formation and high sulphidation mineralization. Figure reproduced from Sillitoe (1994).

9.4 CONCLUDING REMARKS

Kucing Liar holds evidence that porphyry-related deposits are mineralogically and metallogenically zoned and that transitions from one style to the next can be relatively rapid, as seen from the near contemporaneous development of potassic and overprinting quartz-pyrite alteration zones. The results of this research have indicated that the range of porphyry-related deposits, skarn (calc-silicate-magnetite rocks), porphyry (potassic altered rocks), high sulphidation epithermal (quartz ± covellite ± pyrite), carbonate replacement (arsenian pyrite ± chalcopyrite ± covellite) and low sulphidation epithermal (galena-sphalerite ± Au-As-Sb) can form during a single prolonged hydrothermal event. The variations are due to varying degrees of fluid evolution related to cooling and dilution by local water and hence represent relative distance from source in terms of time, space and composition. Interactions with external waters are related to the brittle-ductile transition, which may causes phase separation in the hydrothermal fluid, segregating ore metals between chloride-dominant brines (Fe-Cu-Zn-Pb-Ag) and low density bisulphide-dominant phases (Au-As-Sb). The separation of low and high-density phases at the brittle-ductile transition is expected to facilitate cooling and dilution effects through interaction with local groundwaters. Fault movement localised the conditions required for hydrothermal fluid evolution, in particular the pressure. The study has shown that fault movement and the level of complexity inside the fault system facilitate the local fluid infiltration and may even have some effect on the separation of a hydrothermal phase from magma.

The results were possible because of the detailed nature of data collection, which provided information for building a detailed model of the context of the mineralization as well as allowing comprehensive cross-correlations between mineralogical and geochemical data. Methods exist today for recording and analysing large amounts of data in a full 3-dimensional interactive environment. Observations must be factual rather than subjective to the knowledge and experience of the geologist.